Multiwavelength investigation of PKS 1814-63 as a candidate gamma-ray source

Bachelor Thesis

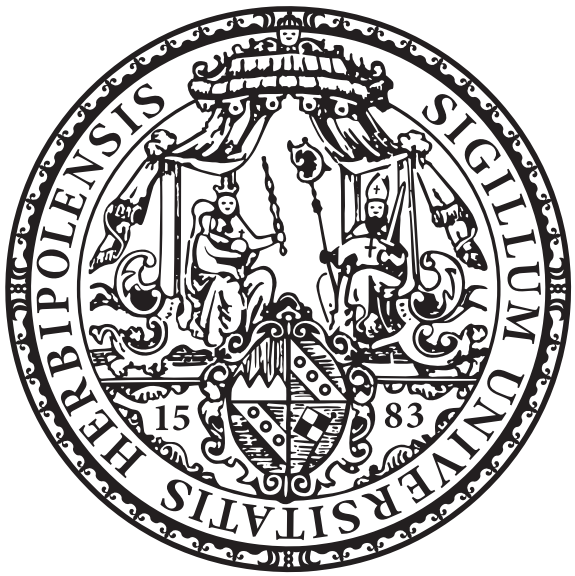

Julius-Maximilians-University Würzburg
Faculty of Physics and Astronomy

Subject:

Physics

submitted by:

Leonard Pfeiffer

February 18, 2022

Supervisor:

Prof. Dr. Sara Buson, Astronomie

Contents

Abstract

Active galactic nuclei (AGN) are the most powerful sources of electromagnetic radiation in the Universe. They are powered by the accretion of matter into the central supermassive black hole. They can be detected at all wavelengths and are therefore the subject of research by satellites from the radio to the gamma-ray band. A few of them develop a relativistic jet, whereby AGN , whose jets are pointing towards earth, are called blazars. Blazars are the most frequently detected sources in the gamma-ray wavelengths. Further distinctions of AGN result from the analysis of the optical spectrum and spectral energy distributions in different wavelengths.
PKS 1814-63 is a very peculiar source as it does not fit into the unification model. Thus, this AGN was tentatively associated by the EGRET satellite as a gamma emitter, whose studies were the first to catalogue many blazars. Previous analyses of data from the *Fermi* Gamma-ray Space Telescope, in contrast, did not confirm this measurement, which is why the question of the classification in the unification model was not fully clarified. Investigations of the optical spectrum led to the assumption of a classification as a Seyfert Galaxy, Narrow-Line or Broad-Line Radio Galaxy by comparison with schematic spectra of different AGN classes. This is also supported by the localization in the BPT diagram by investigating the emission lines H_α, H_β, NII and OIII. The mass of the central black hole which is over $10^8\,M_\odot$ is found to be too high for Seyfert galaxies but fits into jettetd AGN samples. The [OIII] luminosity suggests a low power AGN. This is in great contrast to the findings from the radio wavelengths. Here, PKS 1814-63 shows the characteristics of a powerful jetted Compact Steep Spectrum (CSS)/ Compact Symmetric Object (CSO) AGN. The results obtained here cannot be explained with Seyfert AGN or NLRGs. The young age of the AGN is inferred its classification as CSS/CSO and also by the measurement of outflow material, which influences the growth and the environment of the AGN and possibly contributes to gamma-ray or neutrino production. The result of the subsequent investigation of the spectral energy distribution led to the same classification as the optical spectrum but found increased radio radiation compared to Seyferts. The orientation of the AGN components was determined by comparing optical and radio studies. We carried out a examination of gamma-ray data and could not detect significant emission from PKS 1814-63. By splitting the light curve into equal time intervals, an small improvement in significance (from TS $\simeq 2$ to TS $\simeq 4$) can be detected in one of the four intervals. By analysing the time interval in which the highest detection probability is expected, a test statistic of 6.68 was determined. This corresponds to a significance of $2.10\,\sigma$ for this analysis. As a result of this work, PKS 1814-63 cannot be described by the unification model and shows peculiar properties in the radio wavelengths also due to the presence of an outflow. This could contribute to the production of gamma rays and neutrinos, which is why this AGN remains an interesting object to study in all wavelengths and also for possible neutrino detection.

Zusammenfassung

Aktive Galaxiekerne (engl. AGN) sind die stärksten extragalaktischen Quellen elektromagnetscher Strahlung im Universum. Angetrieben werden sie durch Akkretion von Materie in das zentrale supermassereiche schwarze Loch. Sie sind in allen Wellenlängen detektierbar und daher Forschungsgegenstand von Satelliten von Radio- bis Gamma-Band. Kapitel 1 beschäftigt sich daher zunächst mit der Unterscheidung dieser Objekte. Der Hauptunterschied liegt dabei bei der Existenz eines relativistischen Jets; weitere Unterscheidungen erfolgen dabei durch die Orientierung und die Analyse der optischen und hochenergetischen Spektren.
Diese Arbeit ist durch die kontroverse Klassifizierung von PKS 1814-63 in Katalogen und anderen Veröffentlichungen motiviert. So wurde dieser AGN vom EGRET Satelliten mit einem möglichen Gammaemitter assoziiert, der mit seinen Studien erstmals viele Blazare katalogisierte. Der Satellit *Fermi* konnte diese Messung jedoch nicht bestätigen weshalb die Frage nach der Klassifizierung nicht vollständig geklärt war.
Die Kapitel 2.1 und 2.2 stellen die beiden Satelliten und deren Messgeräte vor, woraufhin in Kapitel 3 bereits veröffentlichte Arbeiten und ihre Erkenntnisse zu diesem AGN miteinander verglichen werden. Der Vergleich des optischen Spektrums mit dem schematischen Spektrum der AGN Klassen führt zur Erkenntniss, dass PKS 1814-63 viele Ähnlichkeiten mit Seyfert Galaxien und Narrow-Line bzw Broad-Line Galaxien (NLRG, BLRG) aufweist. Bestärkt wird diese Vermutung durch die Einordnung in das BPT Diagramm, wobei das Verhältnis der ausgeprägtesten Emissionslinien ebenfalls die beiden Klassifizierungen zulässt. Diese werden anhand der Masse des Zentralen schwarzen Lochs unterschieden, die mit $10^8\,M_\odot$ deutlich höher ist als alle anderen Seyfert Galaxien in einer Vergleichsgruppe. Sie passt jedoch gut zu AGN mit radio-lauten Eigenschaften, deren Masse des schwarzen Lochs auf $10^{8.8}\,M_\odot$ im Durchschnitt angegeben wird. Narrow Line Radio Galaxies zeigen dementsprechend solche Charakterisika. Hier kommt jedoch die intrinsische Luminosität zum tragen, bei der die [OIII] Linie von PKS 1814-63 jedoch nur auf einen schwachen AGN schließen lässt, zu schwach für die NLRGs in einer Vergleichsgruppe.
Im starken Kontrast dazu stehen die Erkenntnisse aus den radio Wellenlängen. Hier weist der AGN starke, radio-laute Eigenschaften und Jets auf. Außergewöhnlich ist dabei die intensive Radioemission aus dem Kern, der zuvor sich als intrinsisch schwach herausgestellt hat. Hierzu gibt es Studien, die einerseits die Interaktion der Jets mit dem Interstellaren Medium (ISM) aber andererseits auch die Interaktion von heißen Partikelwinden nahelegen. Die Partikelwinde haben dabei ihren Ursprung in der Akkretionsscheibe des zentralen schwarzen Lochs und werden durch Strahlungsdruck durch Schockanregungen nach außen gedrängt. Dies beeinflusst die Strahlungseigenschaften des AGN in Form von "outflow" Material, welches zur Bildung von Gammastrahlung und Neutrinos beitragen kann. Im Anschluss zeigt der Vergleich der spektralen Energieverteilung (engl. SED)

mit schematischen SED für AGN für mit und ohne Jet, dass differenzierbare Peaks auszumachen sind, die bei AGN mit starken Jets nicht erkennbar sind, da der Jet das Spektrum dominiert. Die Ähnlichkeit mit Seyfertgalaxien zeigt sich auch in diesem Kapitel, wobei Seyfert 2s die deutlichsten Gemeinsamkeiten zeigen. Jedoch sind in den Radiowellenlängen erhöhte Emissionen auszumachen, weshalb das mit Seyfert 2 eng verwandte Spektrum der NLRG wahrscheinlicher wirkt. Auch die bildgebenden Messungen und Beobachtungen im Optischen und Radio-Band untermauern eine Klassifizierung abseits von Blazar, durch die Ausrichtung der Galaxie und dessen aktiven Kerns. Als solcher wurder dieser AGN wahrscheinlich auf Grund seiner kompakten Emission und dem steil ansteigenden Radio-Spektrum klassifiziert, weshalb PKS 1814-63 im radio Band als Compact Steep Spectrum source (CSS) und als Compact Symmetric Object (CSO) klassifiziert wird.
Um nun zu untersuchen, ob einerseits EGRETs Messung bestätigt werden kann und andererseits zum aktuellen Zeitpunkt Gamma-Strahlen durch die Interaktion im Outflow Material gemessen werden können, wurde im Anschluss eine Analyse der Gammadaten mit Hilfe der Fermitools vorgenommen (Kapitel 4). Diese zeigt, dass die Gamma-Strahlung von PKS 1814-63 nicht zu einem signifikanten Level gemessen werden konnte, da eine maximale Test Statistik von $6,68$ mit einem Richtwert für Detektion von 25 das Ergebnis der Auswertung ist. Dies entspricht im Rahmen der χ^2-Verteilung einer Signifikanz von 2.10σ.
Zusammenfassend kann PKS 1814-63 nicht in das derzeitige Modell für AGN eingepasst werden, stellt aber ein vielversprechendes Forschungsobjekt für Studien an AGN Outflows als Kandidat für die Erzeugung von Gammastrahlung und Neutrinos dar.

1 Introduction to Active Galactic Nuclei

1.1 Structure and classification

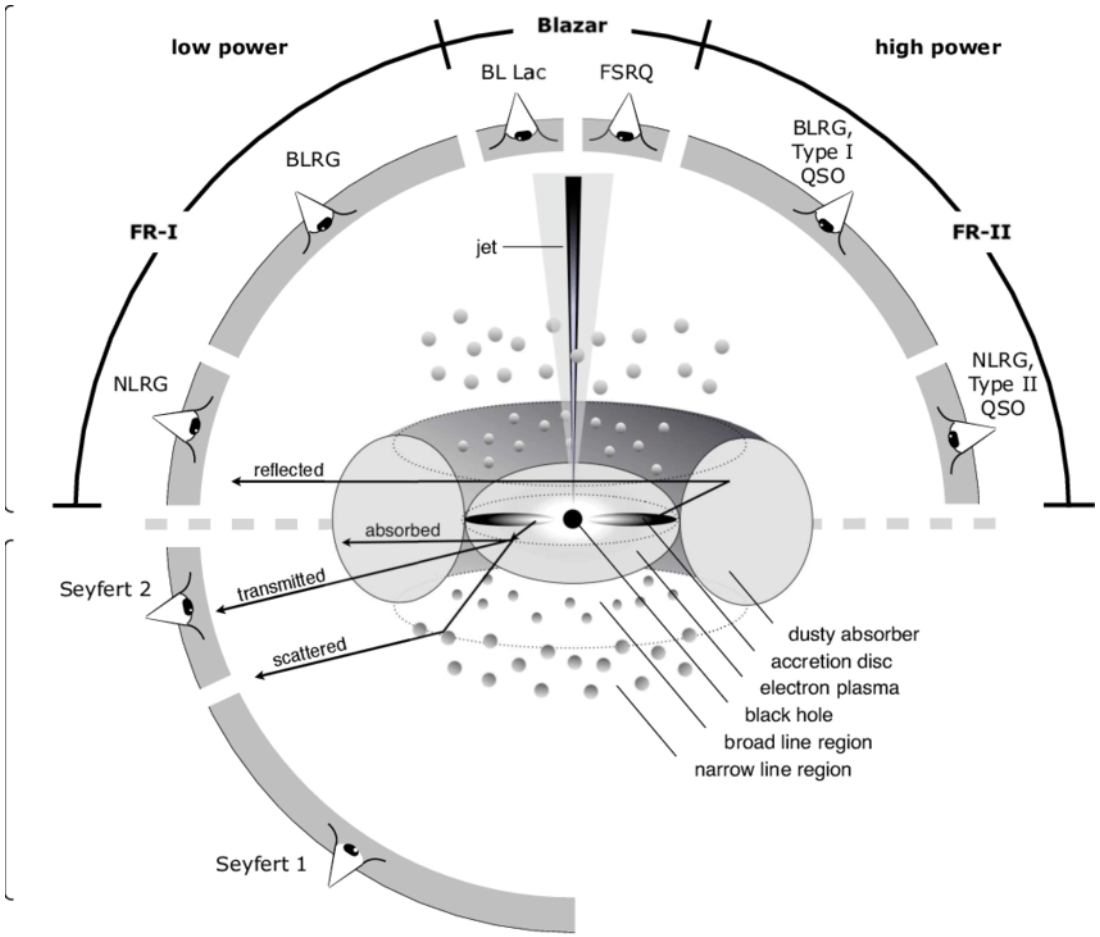

Figure 1: Schematic representation of possible configurations for AGN (not to scale) adapted from Beckmann and Shrader (2013) [1]. The central black hole is surrounded by the accretion disk, which provides matter falling into the core. The emission lines produced in the disk and the corona of the SMBH are obscured by a thick torus of dust depending on the line of sight. There are also accumulations of dust, which are classified as Broad Line Region (BLR) or Narrow Line Region (NLR) depending on their distance from the black hole. They also contribute to the characteristic spectrum of AGN, either through radiation or obscuration.

It is suggested that all giant galaxies have a supermassive black hole (SMBH) at their cores. If these galactic nuclei are powered by accretion of matter, the conversion of gravitational energy from the infalling matter into radiation can generate a huge amount of light, with luminosities that can be higher than the host galaxy itself. These are called Active Galactic Nuclei (AGN) and it further consists of a corona, a accretion disk, a dust torus and in some cases outflowing material and collimated relativistic jets. Close to the

black hole is the corona, which is the name given to the region of charged particles moving in a hot plasma cloud in the vicinity of the event horizon of the black hole. Further out is the Broad Line Region (BLR), presumably made of high speed clouds orbiting the central black hole. This region emits characteristic broad line emission lines in the optical spectrum, which can be affected by the dust torus or the narrow line region, depending on the orientation of the AGN with respect to the observers line of sight. The NLR is further out of the BLR and is therefore always detectable, even if the broad line is obscured. Some AGN also develop a relativistic jet that may extend far beyond the boundaries of the host galaxy. Following the P. Padovani et al. (2017) definition, we distinguish here two main classes that differ in whether or not they form a relativistic jet through accretion [2]. These jets are detectable in all wavelengths from radio to gamma-rays and reach scales from a few astronomical units (AU) to megaparsecs [3], which makes AGN the most powerful and persistent sources of electromagnetic radiation (EM radiation) in the Universe. Since the bolometric luminosity depends very much on the mass falling into the black hole, and the accretion rate is not necessarily constant, one of the most striking characteristics is the high variability within different time scales (from seconds to years). Further, subdivisions in more classes then result from characteristics in the various wavelengths, narrow and broad emission lines and the orientation relative to the Earth. According to Padovani (2017), we therefore distinguish the following characteristics: Quasars, Seyfert 1 (Sey1), Seyfert 2 (Sey2), Radio-loud and Radio-quiet AGN (RL AGN, RQ AGN), jetted and non-jetted, Fanaroff-Riley class I and 2 radio source (FR I, FR II) and Blazars. Further subclasses are shown in figure 1 but will not be discussed here. All of these are described in detail in [4] but for this thesis Seyfert AGN, Narrow Line Radio Galaxies (NLRGs) and Blazars are of particular interest. The following chapter focuses on the physics involved in AGN.

1.2 Physics involved in AGN

1.2.1 Synchrotron radiation

Relativistic jets give origin to high-energy photons. The charged particles move around the magnetic field lines in the jet and lose kinetic energy in form of radiation. If the jet is observed from the side, the EM-spectrum will be multiples of the revolution frequency of the circular particle movement around the jet. The observer will see this as a back and forth motion, comparable to the effect seen in synchrotron accelerators [5]. The synchrotron process emits radiation polarized perpendicular to the magnetic field line, while the charged particle follows the plasma outflow, which forms the jet by moving away from the black hole (Fig. 2). The contribution to the luminosity of the AGN by the

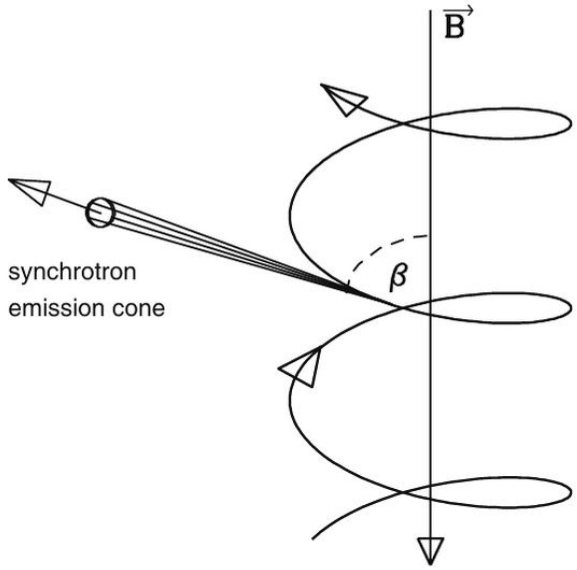

Figure 2: Schematic synchroton emission of a electron with pitch angle β between magnetic field and velocity vector adapted from V. Beckmann and C. Shrader (2012) [6]. The rotation of the electron results in a synchroton emission cone with an opening angle $\Phi \simeq \gamma^{-1}$.

synchrotron luminosity is described by V. Beckman and C. Shrader in [6]. They obtain:

$$\begin{aligned} L_S &= \frac{4Z^4 e^4 B^2 \gamma^2 \nu^2}{9c^5 m^2} \\ &= -\frac{dE}{dt} = \frac{4Z^4 e^4 B^2 E^2}{9m^4 c^7} \end{aligned} \tag{1.1}$$

Since $L \propto m^{-2}$ the equation is most efficient for electrons and positrons if compared to heavier particles like protons. The electrons distribute the flux over a range of energies and contribute to the overall outgoing spectrum. This emission typically follows a power-law energy distribution and is found in several classes of astrophysical sources. It depends directly on the energy of the electrons (E_1 and E_2), so the total synchrotron emissivity expressed by power per unit frequency and per unit volume will be

$$\epsilon(\nu) = \int_{E_1}^{E_2} L(E,\nu)\, N(E)\, dE = k \int_{E_1}^{E_2} E^{-p}\, dE \tag{1.2}$$

with power law index p. The further derivation will not be part of this thesis, for more details, see [6]. One obtains the following proportionality between emissivity and frequency:

$$\epsilon(\nu) \propto \nu^{-\alpha} \tag{1.3}$$

Where α is the spectral index, which can be described by the following expression:

$$\alpha = \frac{p-1}{2} \tag{1.4}$$

The high energy cutoff found in the synchrotron spectrum detectable in AGN is defined by the maximum critical frequency $v_{c,max}$ for most electrons.

1.2.2 Photon scattering

Of interest here are 2 different forms of photon scattering, which differ in their energy scale. The non-relativistic interaction between an electromagnetic wave and a free charged particle is described by Thomson Scattering and was first described by Sir Joseph John Thomson. This process is comparable to fully elastic scattering in classical physics, as the photon and particle will have the same energy afterwards as before. The initial assumption here is that the energy of the photon is significantly smaller than the rest energy of the charged particle. In addition, the kinetic energies must not reach relativistic scales. In the classical sense, the electron is moved by the electric field of the photon, whereby part of its momentum is transferred to the electron. This is reemitted into a photon of the same energy when the speed is decelerated, and depending on the angle relative to the observer it is polarised or not [6]. The differential cross-section of this elastic scattering process can be written as follows.

$$\frac{d\sigma}{d\Omega} = \frac{1}{2}(1 + cos^2\theta)\frac{q^2}{mc^2} \tag{1.5}$$

The symmetry with respect to the angle theta is chosen in such a way that the amount of radiation is the same forwards and backwards and $\frac{q^2}{mc^2}$ is the classical electron radius r_0. This results in the following for the total cross-section:

$$\begin{aligned} \sigma_T &= 2\pi \int_0^\pi \frac{d\sigma}{d\Omega} sin\,\theta\, d\theta \\ &= \frac{8\pi}{3} r_0^2 = \frac{8\pi}{3}\left(\frac{q^2}{mc^2}\right)^2 \end{aligned} \tag{1.6}$$

All photons produced inside a plasma can be Thomson scattered before it continues its way in the direction of the observer, therefore the understanding of this phenomenon is important in many astrophysical sources.
An extension of this principle is described by Compton Scattering, where the momentum of the electron is taken into account in addition to its rest energy. The photon also has a momentum, but no mass. The momentum here depends on frequency and energy: $p = \frac{hf}{c} = \frac{E}{c}$. The law of conservation of energy and momentum then applies also for

massless particles [6]. The energy transfer is directly dependent on the change of direction of the photon. Also the energy of the photon doesn't have to be much smaller than the rest energy of the electron anymore but therefore it is necessary to take quantum mechanical effects into account. They reduce the effective cross-section in comparison to the Thompson case. The energy of the photon after Compton scattering can be derived by:

$$\Delta E = h\Delta\nu = h\frac{c}{\Delta\lambda} \tag{1.7}$$

with

$$\Delta\lambda = \frac{h}{mc}(1 - cos\,\theta) \tag{1.8}$$

This resulting energy after scattering is then:

$$E_2 = \frac{E_1}{1 + \frac{E_1}{mc^2}(1 - cos\,\theta)} \tag{1.9}$$

For the limits of classical physics, where the energy of the photon for scattering (E_1) is much smaller than mc^2, the same case as for Thomson scattering is obtained again, since no energy is transferred to the electron. Taking quantum electrodynamics into account, the cross-section can be described here as in [6], also known as Klein-Nishina formula.

$$\frac{d\sigma}{d\Omega} = \frac{1}{2}\,r_0^2\,f(\epsilon,\theta)^2\,(f(\epsilon,\theta) + f(\epsilon,\theta)^{-1} - sin^2\theta) \tag{1.10}$$

with

$$f(\epsilon,\theta) = \frac{1}{1 + \epsilon(1 + cos\,\theta)} \tag{1.11}$$

ϵ represents E_1, in relation to the rest mass energy of the charged particle. Here, the resulting total cross-section expressed with σ_T and ϵ is:

$$\sigma_{KN} = \frac{3\sigma_T}{4}\left\{\frac{1+\epsilon}{\epsilon^3}\left[\frac{2\epsilon(1+\epsilon)}{1+2\epsilon} - ln(1+2\epsilon)\right] + \frac{ln(1+2\epsilon)}{2\epsilon} - \frac{1+3\epsilon}{(1+2\epsilon)^2}\right\} \tag{1.12}$$

Approximations of this expression show that Compton scattering loses efficiency for high photon energies, also known as the Klein-Nishina effect. This effect therefore has important consequences for the interpretation of the spectral energy distributions of AGN, as it is possible to achieve photon energies in the MeV to TeV range.
The opposite case can also occur, in which an electron moves at relativistic speeds and gives off energy to a photon of low frequency. Since the rest energy of the electron (in relation to the Lorentz factor) is significantly greater than the energy of the photon dependent

on its frequency, the cross-section corresponds to that of Klein-Nishina, providing that the condition for Thomson scattering in the rest frame is met. This type of scattering is called inverse Compton scattering. The luminosity contributed by the inverse Compton effect is proportional to the existing photon density n_{ph}:

$$L_{IC} \propto n_{ph}\gamma^2 E_1 \tag{1.13}$$

The exact derivation of the physics behind the inverse Compton effect is described in various books such as "Radiative Processes in Astrophysics" by G.B. Rybicki and A.P. Lightman (1991) [7] together with the previously discussed radiation and scattering processes. In conclusion it can be said that this process is an important source of X-rays and gamma rays in AGN, since whenever large quantities of photons and relativistic electrons interact, high energy radiation results.

1.2.3 Pair production

In pair production, photons interact with matter or other photons. This process has to obey general conservation laws. In addition to conservation of energy, momentum and angular momentum, the sum of charges must give zero. The result of this interaction is a massive particle, which is why not all results are permitted, but only those in which also the quantum numbers are conserved and the initial products must also carry sufficient energy to allow the final product to have an rest energy of $E = mc^2$ by Einsteins law [6][7]. The product with the lowest mass that can be created in pair production is the electron-positron pair. But this must be in the immediate vicinity of nucleons in order to achieve momentum conservation. The photon energy excess during production is released as kinetic energy. Furthermore, muons, anti-muons, a tau and an anti-tau with corresponding energy can be created. In order to conserve the momentum in all these interactions, it is partly transferred to surrounding particles. This process not only takes place in AGN, but is also important for the detection of high-energy radiation such as gamma radiation. Dense materials are used in detectors or calorimeters to measure the current or "shower" produced by pair production in order to increase the probability for gamma rays to interact with matter. The satellites described in chapter 2 also use this method. In addition to the radiation and scattering processes now described, there are many other effects such as thermal bremsstrahlung and gravitational micro- and macrolensing that influence the luminosity and visibility of an AGN, see [6] and [7].

1.2.4 Hadronic radiative processes

Similar to the leptonic radiation processes explained above, there are also hadronic processes. For this, we now assume a jet in which, in addition to photons and relativistic electrons, there are also relativistic protons and possibly also nuclei with a higher ordi-

nal number. Here, the spectrum produced by synchrotron radiation is also described by a power-law distribution, but the emission is suppressed compared to that of electrons. To compensate this, the magnetic field value, the particle density or both need to be increased. This leads to the hypothesis that proton-synchrotron radiation can be responsible for the high energy component of blazar SEDs, since the synchrotron peak can be expected at $10 - 100\,\mathrm{GeV}$ due to the increased mass of the radiating particle [8].
The protons in the jet also interact with matter and the photon field at their surroundings, photons generated by the synchrotron radiation of electrons. The previously mentioned inverse Compton effect is the dominant radiation effect for electrons, but is so small for protons that in principle it can be negated for AGN. Much more important for gamma-ray emission is the lepto-hadronic pair production, which can happen through interaction with photons, there is the possibility of photo-meson (photo-pion) production. An example of such a reaction chain is:

$$p + \gamma \rightarrow n + \pi^+ \tag{1.14}$$
$$p + \gamma \rightarrow p' + \pi^0 \tag{1.15}$$
$$p + \gamma \rightarrow p' + \pi^+ + \pi^- \tag{1.16}$$
$$\pi^0 \rightarrow 2\gamma \tag{1.17}$$
$$\pi^+ \rightarrow \mu^+ + \nu_\mu \rightarrow e^+ + \nu_e + \bar{\nu}_\mu + \nu_\mu \tag{1.18}$$
$$\pi^- \rightarrow \mu^- + \bar{\nu}_\mu \rightarrow e^- + \bar{\nu}_e + \nu_\mu + \bar{\nu}_\mu \tag{1.19}$$

Accordingly, not only photons but also neutrinos are produced, which can leave the emission region unimpeded. If these neutrinos are detected on Earth, they are a smoking gun of the existence of relativistic protons in the jet of the corresponding source. In addition to neutrinos, this reaction chain also contributes to the injection of electron-positron pairs in the region. For a detailed explanation and derivation of which energies are produced in these reactions and how the radiative components are composed, see M. Cerruti (2020) [8]. Also derived there is the Bethe-Heitler pair production, which competes for small energies, but which is not discussed separately because of its strong similarity to the one already discussed. In general, leptonic models sufficiently describe AGN radiation processes, as pure hadronic models are difficult to maintain due to the high proton density required. Nevertheless, lepto-hadronic processes are possible at appropriate energies and therefore also contribute to the total emission, especially at high energies.

1.3 Seyferts, NLRGs and Blazars in different wavelengths

The major difference between Seyferts, NLRGs and Blazars is the orientation. While blazars have a jet oriented close to the line of sight with a alignment of 0° up to 20°, one is looking at higher tilt angles up to the line of sight with the dust torus in the case of

Seyfert cores. A general distinction is made between Type 1 and Type 2 AGN, which are also shown in Fig. 1. It should be noted that the orientation of the galaxy and the AGN seem to be physically related, but exceptions were found, so considering the galaxy as a whole always makes sense but cannot be used as an argument for definite classification. In the observation of astrophysical sources, different satellites cover different ranges of the electromagnetic spectrum. AGN are therefore selected and classified in the following wavelengths:
In the radio wavelengths, it is investigated whether an AGN has a jet and whether radio radiation is emitted from the immediate vicinity of the SMBH. A distinction is made between radio-loud and radio-quiet AGN, which are divided according to the ratio of the radio flux (in 5 GHz) and the optical flux (in the B-band):

$$\frac{F_{5\,\mathrm{GHz}}}{F_B} \geq 10 \tag{1.20}$$

So if this ratio is greater than or equal to 10, AGN are described as radio loud, which is often but not always equivalent to the presence of a jet, but AGN with a jet are radio loud. Blazars and Narrow Line Radio Galaxies have these jets and are radio-loud; Seyfert Galaxies, on the other hand, are usually not detectable on the radio, or at least no jets are detectable, and are radio-quiet. Infrared radiation is mainly due to thermal emission from the dust in the vicinity of the SMBH. In the case of blazars, the jet usually outshines most of this emission; in the case of NLRGs, it depends on the intensity of the jet, while in the case of Seyfert, the components in the spectral energy distribution are distinguishable. Different classes of AGN also show different characteristics in the optical spectrum. Some classes can be divided by their emission lines, while others can be identified by the general shape of the spectrum. This will be discussed in more detail in chapter 3.1. The high-energy radiation, must be distinguished according to its origin. AGN represent only a small number of galaxies, and an even smaller percentage of them have a jet that in a few cases is directed towards us. In the case of no jet, the X-ray emission comes from the hot corona of the SMBH, also visible in Fig. 3. The corona emission can be detectable up to the MeV range and describes the highest possible energies for AGN of this type. In the case of a jet, the jet also outshines this component. The highest photon energies are reached by blazars, which can be (but do not have to be) measured in the SED up to the high gamma-ray range. In the case of NLRGs, it also depends on the intensity of the jet whether the radiation reaches gamma-ray wavelengths. If the jets in the case of an NLRG are weak or absent, as in the case of the Seyfert galaxy, X-rays from the corona in the vicinity of the SMBH are still detectable. A typical spectral energy distribution AGN is also shown in Fig. 3, which distinguishes between jetted and non-jetted AGN. How much a jetted AGN outshines the galactic components with its jet depends on whether it is a low synchrotron peaked (LSP) or a high synchrotron peaked (HSP) AGN, more

specifically distinguished in Fig.4. The distinction between these two types comes from the initial energy of the electrons / protons involved in the radiation, but follow the processes explained in chapter 1.2.
Apart from the spectrum, the bolometric luminosity also differs between the different AGN classifications. Of the three, Seyfert galaxies have the lowest bolometric luminosity. In NLRG, a distinction is made between high and low power, which closely correlates with the intensity and size of the jet. On average, blazars show the highest bolometric luminosity, since the jet, which is oriented nearly directly towards us, has a large influence on it. Low power NLRGs are closely related to Seyfert 2 galaxies under these considerations and show similar curves and peaks in the optical spectrum and the energy distribution of higher energies. The difference between these two classes is found in their radio properties. If a galaxy that could be a Seyfert galaxy in terms of orientation and other characteristics is detected as having a jet in the radio, which would classify it as a radio loud, then the ”radio loud Seyfert 2 galaxies” are low power NLRGs (and the ”radio loud Seyfert 1 galaxies” are low power Broad Line Radio Galaxies (BLRGs)).
The observed properties of AGN that led to a classification may be very variable, especially in case of jets and so their classification must be variable as well. In particular, Seyfert galaxies can also have had a jet at one time or develop one in the future, whereupon they have to be classified again. After the introduction of the AGN classes that are important for this work, the following chapter is about two telescopes that have been used in the analysis of the source.

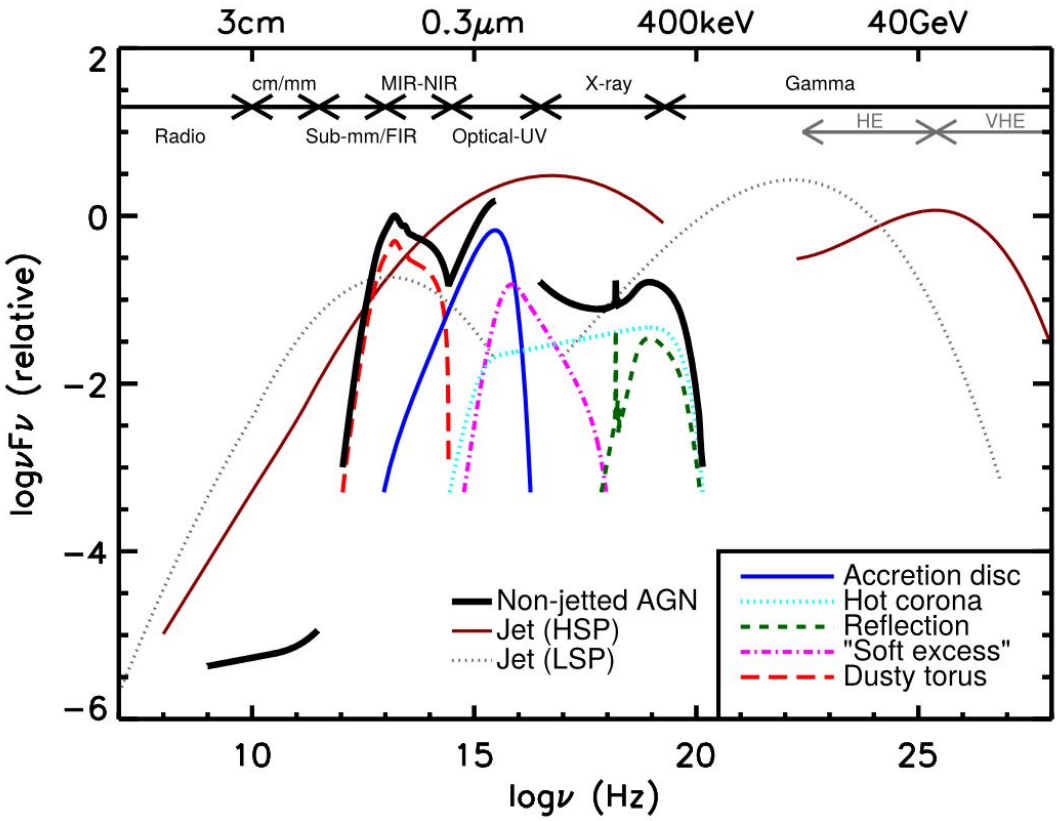

Figure 3: Schematic spectral energy distribution of AGN adapted from P.Padovani et al. (2017) [2]. The SED of different AGN types are compared here. The black line represents the total SED of a non-jetted AGN, consisting of the coloured lines enclosed by it, which take into account the emission of different components. The large red line shows the SED of a high synchrotron peaked (HSP), jetted AGN. The grey dashed line matches the low synchrotron peaked (LSP), jetted AGN.

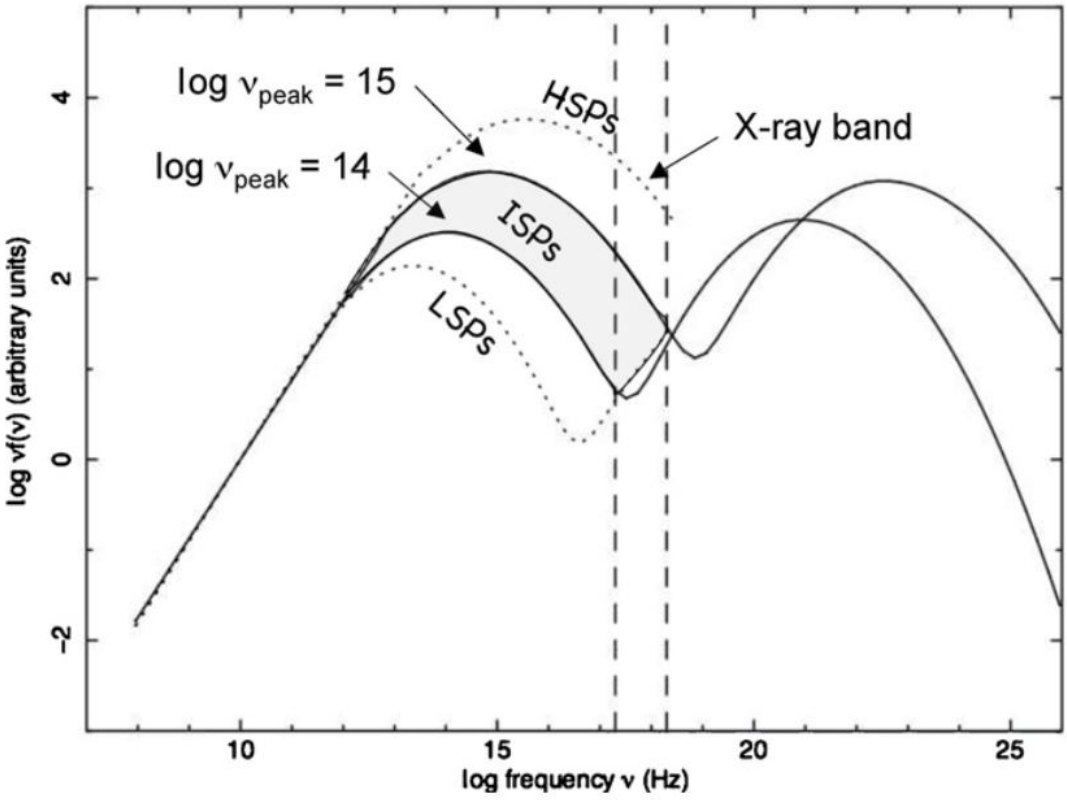

Figure 4: Differentiation of different blazar types based on their synchroton component in the SED, adapted from Abdo et al. (2010) [9]. Two humps can be identified, the first between UV and X-ray frequencies, which can be assigned to synchrotron effects. The origin of the second hump is not yet known. There are therefore 3 subclasses to distinguish, depending on the position of their synchrotron peak.
Low synchroton peaked (LSP) AGN: $\nu_{peak} < 10^{14}\,\mathrm{Hz}$
Intermediate synchroton peaked (ISP) AGN: $10^{14}\,\mathrm{HZ} < \nu_{peak} < 10^{15}\,\mathrm{HZ}$
High synchroton peaked (HSP) AGN: $\nu_{peak} > 10^{15}\,\mathrm{Hz}$

2 Gamma-ray observatories

2.1 The Energetic Gamma Ray Experiment Telescope: EGRET

The Energetic Gamma-Ray Experiment Telescope (EGRET), was designed to detect gamma rays in the range 30 MeV-30 GeV. It was part of the Compton Gamma Ray Observatory (CGRO) and started its mission in 1991. In 2000, due to problems with one of CGRO's gyroscopes, the mission ended in a controlled destruction by re-entry into the atmosphere. One of the main scientific objectives of the telescope was to make all-sky surveys and find high-energy gamma-ray sources. During these surveys, EGRET identified blazars that were already predicted to be gamma emitters by radio and optical observations and new sources.
The structure of EGRET can be found in Fig. 5. The anti-coincidence systems, consisting of a scintillation dome and the time of flight coincident system efficiently filtered unwanted events that could be misinterpreted with gamma rays. The spark chamber, consisting of intervaled tantalum foils and tracking layers, was designed to capture a fraction of incoming gamma rays, where interaction with the constituents created high-energy positron-electron pairs whose movement through the layers was tracked, allowing measurements to be made of the direction of the incoming radiation. At the bottom of the tracker, these were then absorbed by the Total Absorption Shower Counter (TASC). TASC was a NAl(TL) calorimeter used to measure the energy of the incoming pair-produced particles. The reconstruction of an event therefore required the following measurements. The scintillation dome measured the number of particles, the calorimeter the energy of the particle and the spark chamber the direction, together with the detection time.
The sensitivity of EGRET was studied via Monte Carlo simulations [10]. It was found that the sensitivity is not high enough to detect 100 percent of the polarised gamma rays. An improvement of the sensitivity could not be achieved during the mission, but the experience of EGRET was used to develop better detectors with a larger effective area as the *Fermi*-LAT.

2.2 The *Fermi* Gamma-ray Space Telescope

The *Fermi* Gamma-ray Space Telescope (FGST) has two main instruments specialized in the detection of high-energy photons. The primary instrument called Large Area Telescope (LAT) in Fig. 6 is an imaging telescope for photons for energies of 20 MeV to more than 300 GeV. The secondary instrument is the γ-ray Burst Monitor (GBM), which measures mainly transient phenomena in the 8 keV to 40 MeV range. In 2008 *Fermi* began to take data in a circular orbit around the Earth at an altitude of about 565 km and an inclination of 25.6 deg with respect to the equator.The Earth's magnetosphere partially protects the observatory from cosmic radiation. In its primary working mode, the so-

called scanning mode, LAT observes the entire sky every 3 hours. Random events and interference from the charged background are largely identified by the anticoincidence detector (ACD) (Fig. 6), similar to EGRET. Its special design of plastic scintillator tiles achieves 99.97% efficiency in rejecting individual charged particles. After the gamma radiation has passed the ACD, it penetrates the tracker material. In this case, the gamma-ray interaction with tungsten results in the production of electron-positron pairs whose trajectories are detected in the instrument. This "shower" then triggers more reactions. In order reconstruct the event direction to a region in the sky, the tracker combines hits that are spatially close together and determines their 3-dimensional position in the detector. To detect the energy of the incoming gamma ray, a calorimeter made of 96 CsI crystals doped with thallium is installed. Through specially arranged photon diodes around the crystals, both longitudinal and transverse information about the energy distribution pattern is obtained during a particle shower. Since each crystal also provides information about its own position in the lattice and light yield symmetry, a calorimeter can measure the emitted energy of the shower and its evolution. This enables the estimation of the energy loss and a distinction from hadronic showers (produced by, for example, most cosmic rays). Together with two algorithms that take into account the centroid axis on the one hand and the energy distribution in the calorimeter on the other, the arrival direction and total energy of the photon are established.
The first analysis of the data collected takes place on board the satellite. The Data Acquisition System (DAQ) combines the information from the other subsystems and reduces the trigger rate ($2-3$ kHz) through filters to a downlink rate of ~400 Hz. Only ~$2-5$ Hz of this are astrophysical photons. The procedure can be found in [11]. Based on Monte Carlo simulations, the Instrument Response Functions (IRF) were developed for the LAT. The IRFs provide the instrument performance as a function of photon energy, incidence angle, conversion point within the instrument for data analyses. A classification and background rejection labels are assigned to each event in the final dataset, which ensures a high accuracy of the event direction and energy. What remains is a table consisting of the event time, the energy, the event direction and other related data.

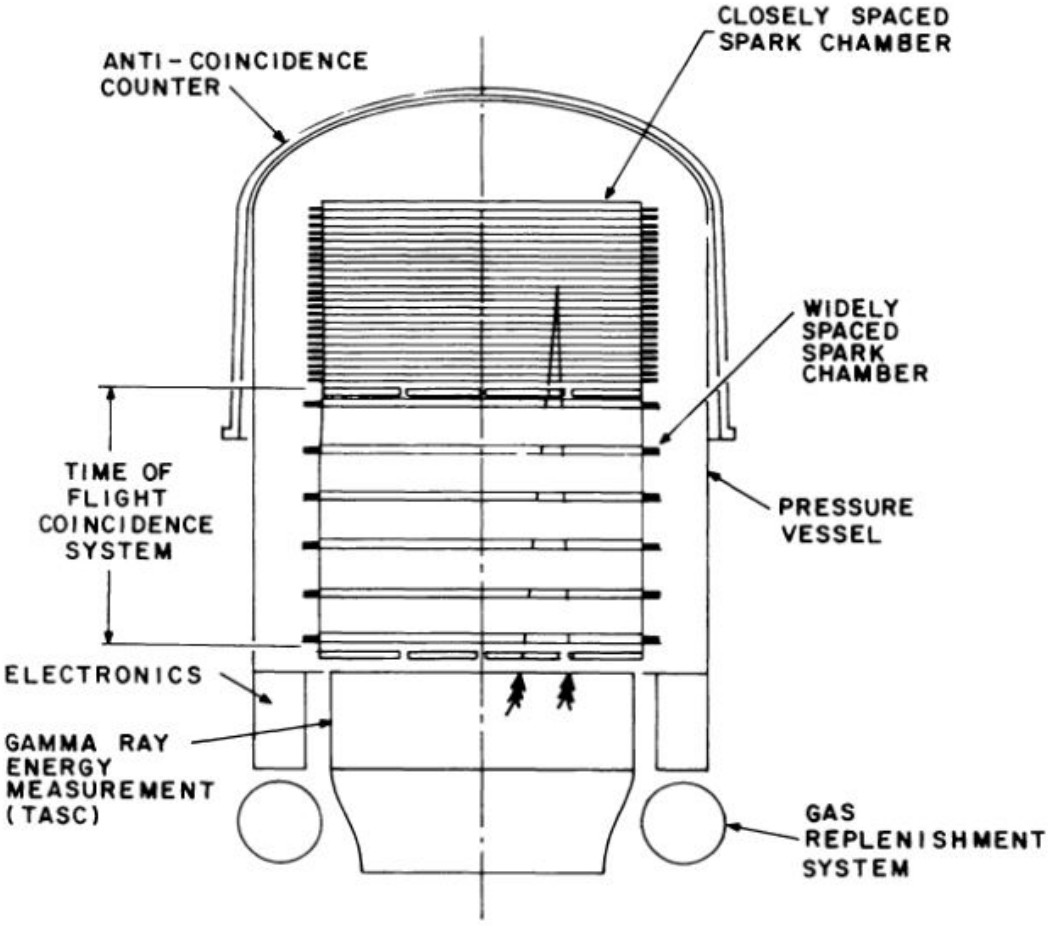

Figure 5: Schematic arrangement of EGRET components, adapted from G. Kanbach et al. (1989) [12]. The individual components were: An anticoincidence system to discriminate charged particles; the spark chamber with several layers of conversion material materialises photons into electron-positron pairs and thereby predicts their arrival direction; a total absorption spectrometer crystal (TASC) calorimeter made of NaI to measure energies.

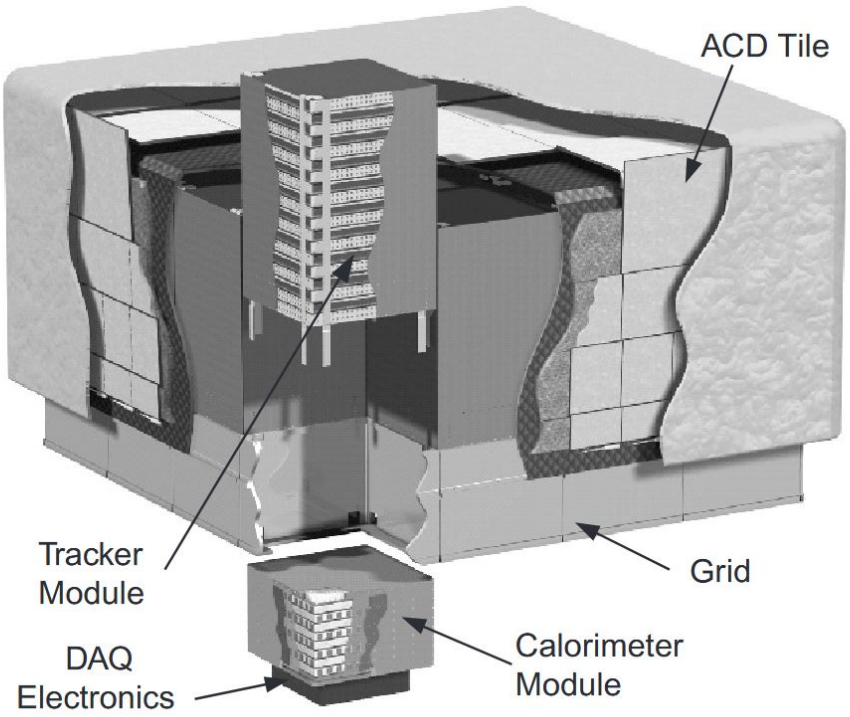

Figure 6: Schematic view of the LAT adapted from R. P. Johnson and R. Mukherjee (2009) [13] including a 4×4 array of towers inserted in an aluminium grid. The tracker array is covered by the ACD. Under each of these converter-trackers is a calorimeter module with the tower electronics module (TEM) beneath them. The TEM consists of a programmable trigger and the Data Acquisition System (DAQ).

3 Previous works and physical properties of PKS 1814-63

Before analysing the possible gamma-ray emission from PKS1814-63, the following chapters deal with the physical properties of the source in other wavelengths, starting with the optical spectrum. This serves to possibly narrow down the AGN classes that can be considered for this source and to better understand the processes that take place in this peculiar source.

3.1 Optical spectrum

The optical spectrum of this source is taken from F. Santoro et al. (2002) [14] and shown in Fig. 7,in which the redshift of PKS 1814-63 of z=0.06373±0.00002 has already been corrected. The upper panel shows the so-called UVB+VIS spectrum of the galactic

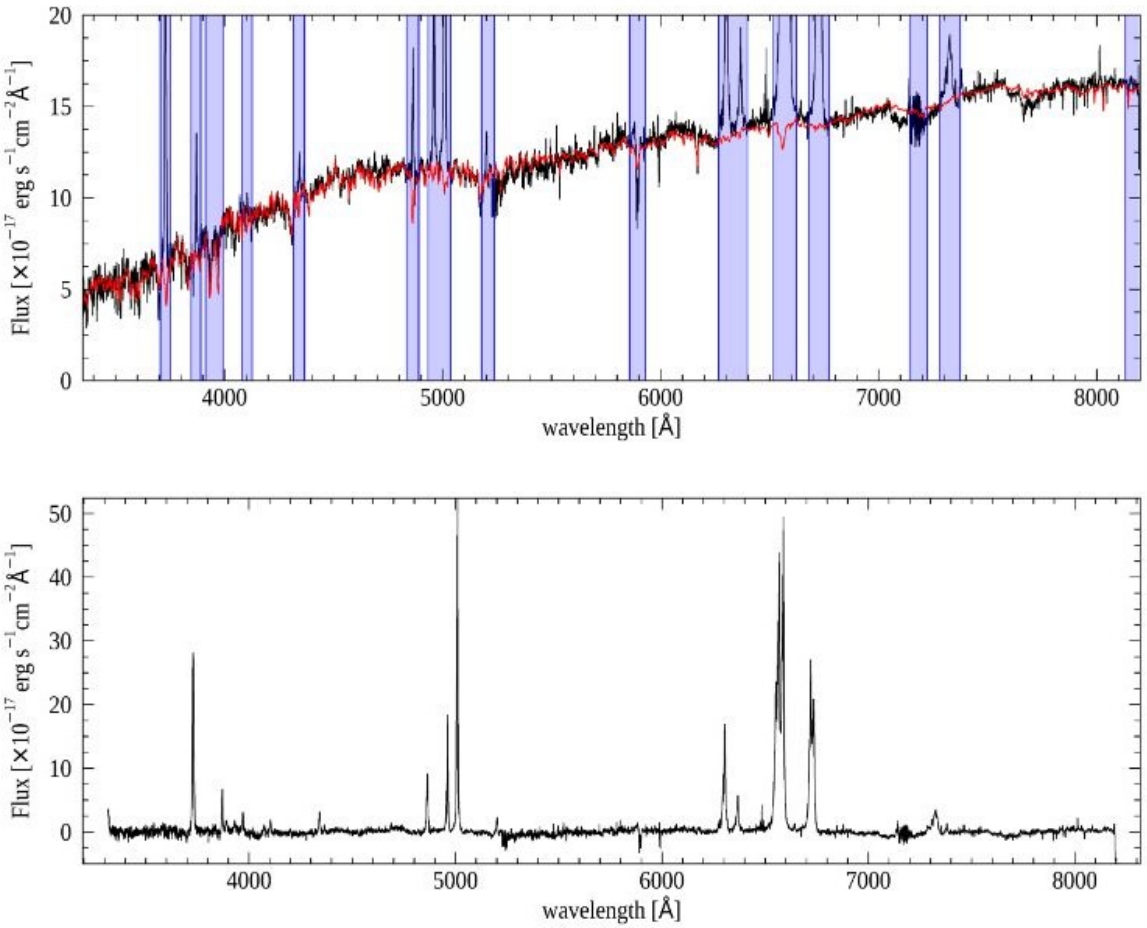

Figure 7: Optical spectrum of PKS 1814-63 adapted from F. Santoro et al. (2020) [14]. The upper panel shows the UVB+VIS spectrum of the galactic nucleus (black line) overlaid with its best-fit model (red line) for the continuum emission. The areas marked in blue correspond to masked emission. The lower panel shows the residual spectrum after subtraction of the stellar continuum.

nucleus, which is overlaid by a best-fit model for the galactic emission. The difference between the two is shown in the residual spectrum in the lower panel. For the classification into an AGN class, the lower panel is of particular interest. The spectrum shows very strong lines of ionised gas indicating the presence of the AGN. The overall shape of the optical spectrum usually already gives a good indication for the classification of the AGN. For this purpose, spectra of other AGN, which can be found in Fig. 8, were compared with the spectrum of PKS 1814-63. Three spectra in this representation share common features

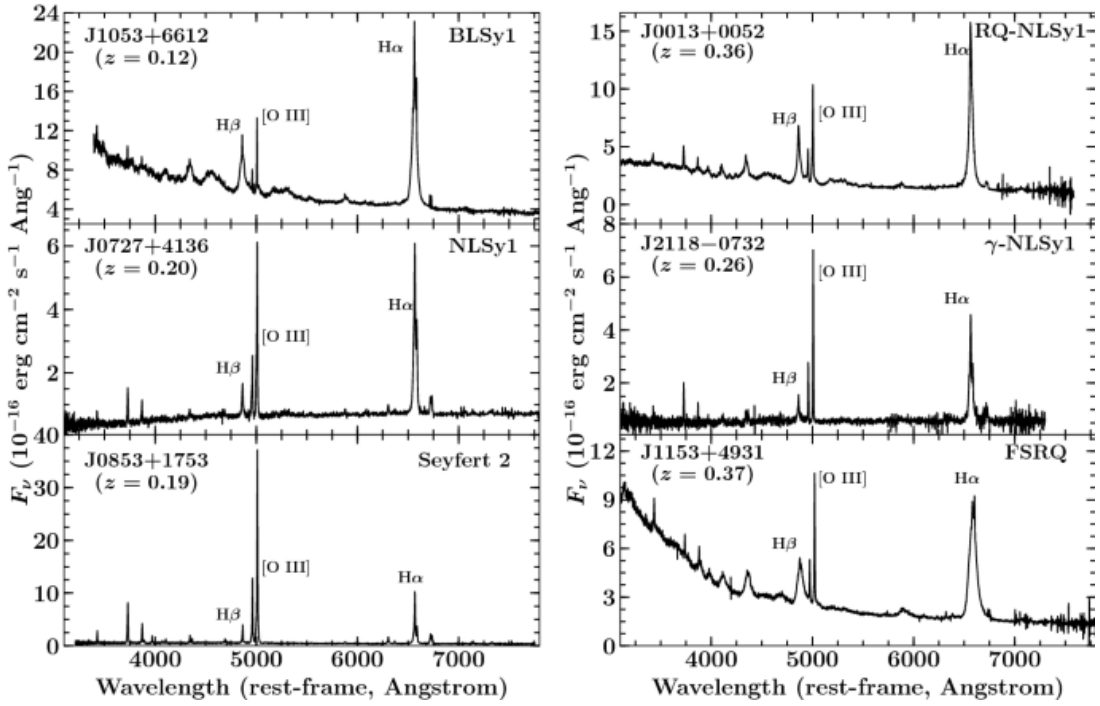

Figure 8: Typical optical spectra of different AGN types adapted from Vaidehi S. Paliya (2019) [15]. The classifications follow the scheme described in chapter 1. The additional specialised cases are BL (Broadline), NL (Narrowline) and RQ (Radio quiet).

with the optical spectrum of PKS 1814-63.These are Narrow Line Seyfert 1 (NLSy1), a subtype of Seyfert 1 Galaxies with high variability, γ-NLSy1 and Seyfert 2 AGN, so we think that one of these classifications may apply to our target. Furthermore there are other classifications that may apply to this source as NLRG and BLRG spectra, for example shown by Rafael Costero and Donald E. Osterbrock (1977) [16], also show a development comparable to that of Seyfert galaxies. Neither FSRQ, nor BL LAC (not shown in Figure 8) qualify. FSRQ display a prominent drop from high flux values in the blue continuum, which is not found in Fig. 7. The optical spectrum of a BL LAC usually does not have this drop and maintains its high flux value, which is why only in a few cases emission lines are visible. The NLSy1 shows a slight increase at the beginning, which could also not be observed here. But the increase is so small that this alternative cannot be ruled out for now. The γ-NLSy1 has many similarities, but is characterised, as the name suggests,

by a variable gamma emission, which is investigated in chapter 4.2. Lastly, the Seyfert 2 spectrum also shows many similarities with the optical spectrum shown here. One difference are the more pronounced H_α and [NII] emission lines in the case of PKS 1814-63. Prominent emission lines affect the classification of AGN, as shown in Fig. 9. This

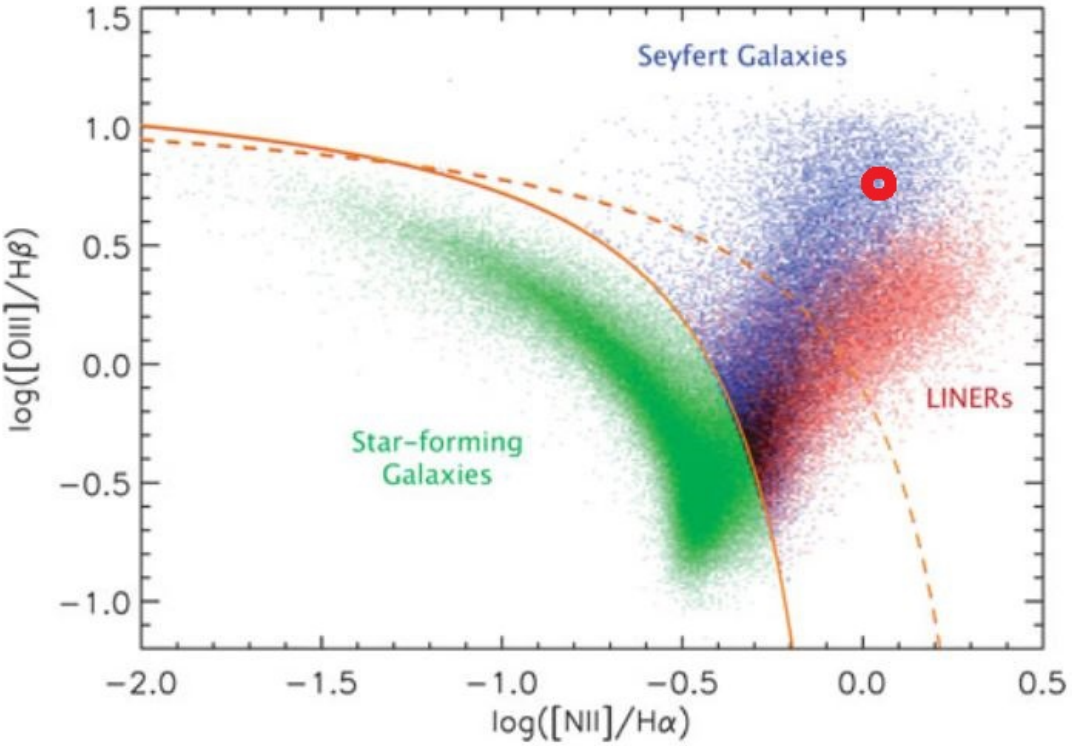

Figure 9: Spread of emission-line galaxies from the Sloan Digital Sky Survey (SDSS) on the line ratio diagnostic diagram adapted from Phillips Baldwin and Terlevich (1981) [17]. It compares strong optical emission lines, in this case [NII] at 6583 $\mathring{A}$ with H_α at 6563 $\mathring{A}$ and [OIII] at 5007 $\mathring{A}$ with H_β at 4861 $\mathring{A}$. The orange lines indicate the empirical (solid) and the theoretical (dashed) border between emission of star forming galaxies and the AGN emission.

BPT diagram compares the ratio of emission lines for different galaxy and AGN types. The ratio of the [NII] line at 6583 $\mathring{A}$ and the H_α line at 6563 $\mathring{A}$ for our spectrum has a value of $\log([\text{NII}]/\text{H}\alpha) = 0.04$, so this AGN falls to the positive part of the x-axis based on the logarithmic plot. This excludes a classification as a star-forming galaxy. The ratio of the [OIII] line at 5007 $\mathring{A}$ and the H_β line at 4861 $\mathring{A}$ has a value of $\log([\text{OIII}]/\text{H}\beta) = 0.76$. Therefore, the y-value of the AGN is also positive and PKS 1814-63 is assigned to high y-values and thus to Seyfert galaxies, which is also consistent with the observations made earlier by comparison. The position of PKS 1814-63 in the BPT diagram is represented by the red area in Fig. 9. In general, quazars occupy the same region as Seyfert galaxies within this BPT diagram. The distinction can be made by comparing the black hole mass. For PKS 1814-63 it is $3 \cdot 10^8$ up to $10^9\,M_\odot$ [18] which is higher than any other Seyfert

galaxy of the comparison sample in the publication but it fits well into radio-loud/jetted AGN samples as they are expected with black hole masses of $10^{8.8}\,M_\odot$ on average. So also for NLRGs and BLRGs this would be within the range, which is why further investigations are necessary to be able to make a statement about the classification of this AGN. The following chapter deals with the properties of PKS1814-63 in the radio wavelengths.

3.2 Radio observations

Results in the radio band provide information about the morphology of the AGN. There are several studies using Very Long Baseline Interferometry (VLBI), some studies that also include PKS 1814-63. These are listed together with the results of the TANAMI studies (Tracking Active galactic Nuclei with Austral Milliarcseccond Interferometry) in the following table.

Study	Year	Classification	Reference
VLBI	2002	CSO	[19]
TANAMI	2010	CSS	[20]
TANAMI	2016	None	[21]
VLBI	2018	None	[22]
VLBI/TANAMI	2019	CSS/CSO	[23]
VLBI/TANAMI	2020	CSS/CSO	[24]

In the radio band, PKS 1814-63 is thus classified as a Compact Steep Spectrum (CSS) source and Compact Symmetric Object (CSO). CSS AGN are radio-loud with a steeply increasing spectrum in the $50 - 100\,\mathrm{MHz}$ range and are therefore more likely to be young jetted AGN. The classification CSO confirms the assignment of a young age for PKS 1814-63 ($\leq 10^4\,\mathrm{yr}$, G. B. Taylor and A. B. Peck (2003) [25]), since these sources have less than 1 kpc in size and additionally show strong symmetries (no or only weak irregular features in radio emission). In connection with this classification, PKS 1814-63 also appears in blazar catalogues such as BZCAT [26]. Whether sometimes CSS AGN are misclassified as blazar, due to similar compact spectra and peaks in the GHz range is part of the work of Ryosuke Itoh et al. (2020) [27]. It is described that blazars can be distinguished from CSS sources by the existence of a peak in the ~ GHz range, which was not further investigated here for the time being, as it is not found in the SSDC Spectrum in chapter 3.4.
Due to the resolving power of TANAMI in the order of a few milliarcseconds, the immediate vicinity of the AGN was mapped in 2008 in a wavelength of 8.4 GHz (Fig. 10). In addition to the compact radio emission in the centre, two lobes are visible here, aligned

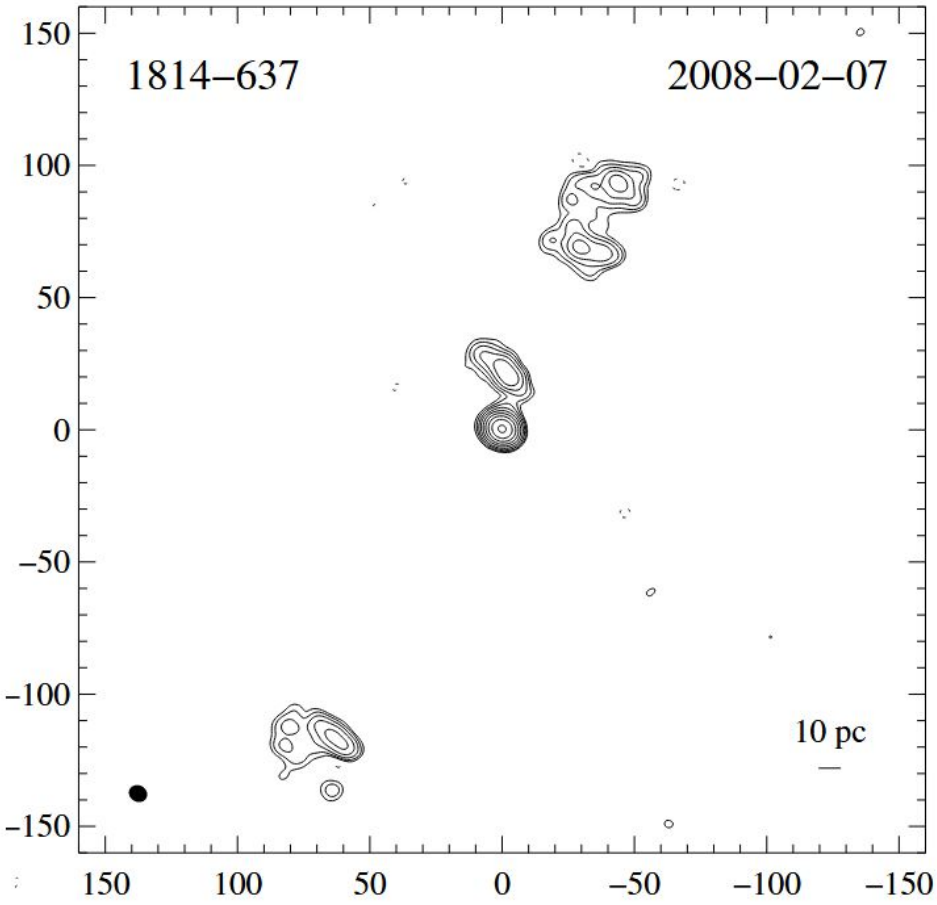

Figure 10: Contour map of PKS 1814-63 at $8,4\,\mathrm{GHz}$ in a scale of milliarcseconds adapted from R. Ojha et al. (2010) [20].

from south to north. These are probably hotspots of an active jet, whose radiation between the hotspots and the black hole is only not visible due to the high sensitivity required for this. This orientation would be unusual for a blazar based on Chapter 1.3, but since blazars are classified primarily by their optical spectrum and high spectral energy distribution, the orientation cannot be used as the primary argument for exclusion. This is supported by exceptions such as the Blazar 3C 273, whose jets are also not directly aligned with the observer and effects such as jet bending (M. Karouzos et al. (2012) [28]) and a realignment of the jets (J. F. Helmboldt et al. (2008) [29]) that would allow a classification as a blazar. However, it would be very unlikely to find these effects to such an extent for this source, as the resulting deviation is usually assumed to be only a few degrees.

These images show that PKS 1814-63 is a powerful radio source with comparatively small jets but a strong emission in the core with a measured radio power of
$\log \mathrm{P}_{5\mathrm{GHz}} = 26,54\,\mathrm{W\,Hz^{-1}}$ [30]. Also the bolometric luminosity of PKS 1814-63, published by F. Santoro et al. (2020) [14] of $L_{L09} = (8.1 \pm 3.2) \cdot 10^{43}\mathrm{erg} \cdot \mathrm{s}^{-1}$ and $L_{H04} = (1.2 \pm 0.1) \cdot 10^{44}\mathrm{erg} \cdot \mathrm{s}^{-1}$, is consistent with radio-loud AGN samples. The two values result

from different calculation methods. L09 represents the calculation according to Lamastra et al. (2009) [31] and H04 according to Heckman et al. (2004) [32].
In addition, two hotspots are recognisable. Further important findings are provided by a publication by R. Morganti et al. (2011) [18], as they also dealt with the question of the origin of the strong radio emission in a galaxy that is optically more like Seyfert galaxies. A possible explanation for this phenomenon is provided by the optical morphology of the AGN and the galaxy, which are discussed below.

3.3 Optical imaging and particle interactions with dust

Optical images of PKS 1814-63 were published by C. Ramos Almeida et al. (2011) as part of a study with the Gemini Multi-Object Spectrographs, which deals with broad-band images for 46 stellar 2Jy radio galaxies [33]. As can be seen in Fig. 11, the galactic centre is crossed by a dust lane of ~20 kpc in diameter that provides irregular features at the outer ends of the disk of the galaxy. This suggests that we are not looking perpendicularly at the galactic disk, but rather it is oriented so that it is perceived as a dust line, which means nearly lateral. For an overall overview of the source, compare the optical image in Fig. 11 with the radio image in Fig. 10, taking into account the different scaling and orientation of the morphologic features.

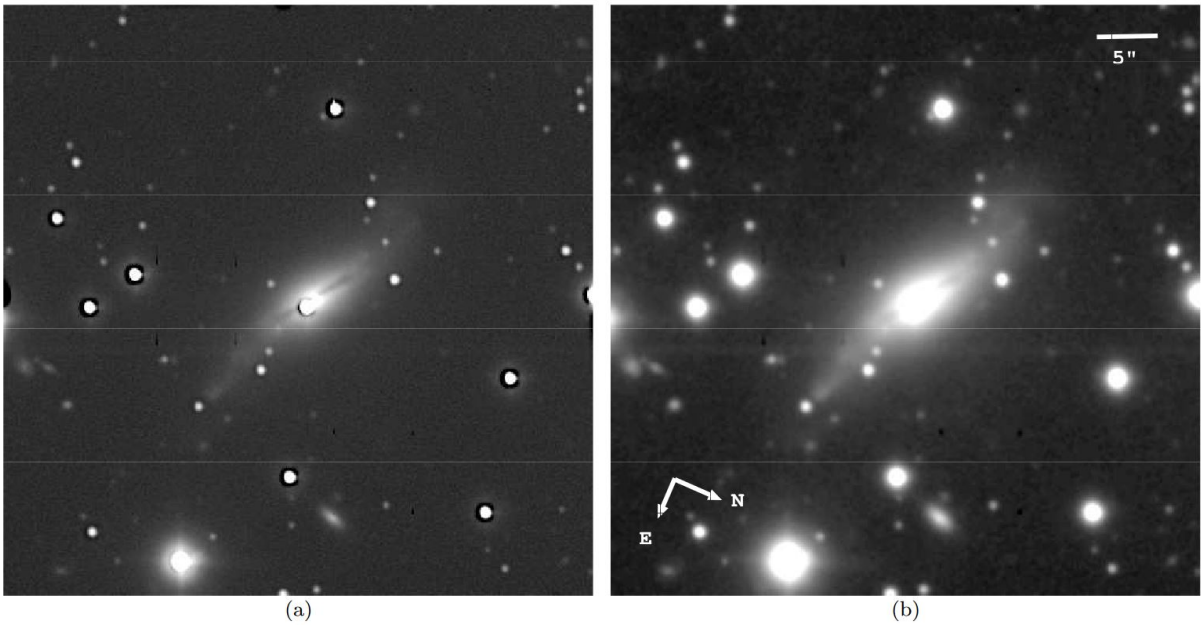

Figure 11: Image of the detection of dust and morphologic features in the Galaxy PKS 1814-63 adapted from C. Ramos Almeida et al. (2011) [33]. (a) Shows the unsharp-masked image with a moving box of five pixels in width. (b) Shows the median filtered image using a 5 five pixel box in width.

Fig. 12 shows this comparison. The orientation of the AGN relative to the galactic plane

reinforces possible classification as NLRG or Sy2. A possible interpretation is that we do not seem to be looking at the galaxy exactly from the side, but maybe in such a way that the AGN is slightly tilted in our direction of view, so that this angle between dust lane and lobes is formed. This dust belt was also discussed by Morganti et al. (2011) [18] as a possible cause for the strong, compact radio emission in the centre. Thus, due to the very pronounced dust, there could be prominent interactions and an efficient conversion of jet power into radio emission. This is supported by their investigation of the L [OIII] luminosity, which is a good indicator for the intrinsic power of an AGN. PKS 1814-63 has a [OIII] luminosity of $L_{[OIII]} \simeq 6 \cdot 10^{41}\,\mathrm{erg \cdot s^{-1}}$, which is the lowest value compared to the 2Jy sample of NLRGs used there [18]. This makes this AGN a very peculiar source. The intrinsically weak AGN with high power in radio would therefore neither fit the definition of a Seyfert nor a classical NLRG.

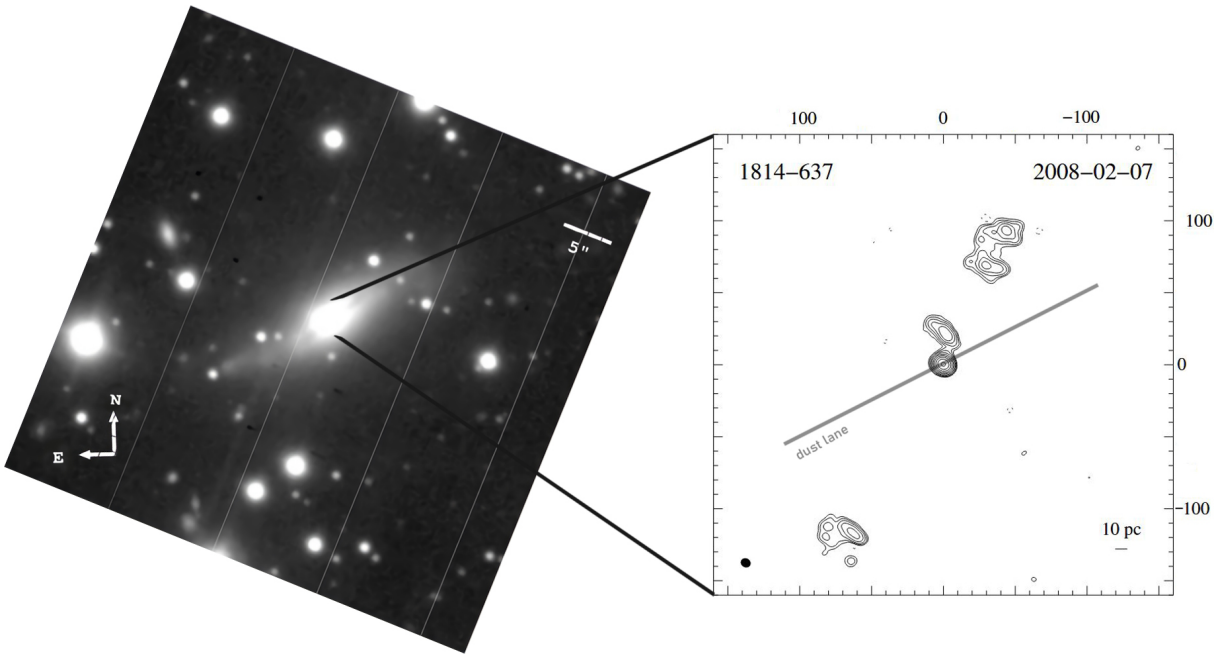

Figure 12: Comparison of orientation and scale of the radio and optical morphology of PKS 1814-63. The original pictures were adapted from [33] and [20] and edited by Bruno Dulcimascolo.

One possibility of interaction with the Interstellar Medium (ISM) is the subject of the publication by F. Santoro et al. (2020) [30]. They describe the measurement of the expansion of young radio galaxies through the interstellar medium. Thus, in addition to the jet interaction that provides the outflow material, there is also the explanation that the hot particle winds produced by accretion interact with the ISM through radiation pressure. Which of the two processes contributes to what extent has not yet been proven, but the outflow material could be measured and its velocity determined, which according to extrapolations will never be on relativistic scales for this source [30]. Not only winds

close to the speed of light contribute to hadronic radiation effects, for example described by M. Ajello et al. (2021) [34], but also large scale winds far below these speeds can cause such reactions is described by P. Padovani et al. (2018) [35]. Thus, the particle winds do not affect the outflow material constantly, but excite it in shocks, whereby the charged particles could have sufficient energy to be able to engage in lepto-hadronic interactions. Consistent with chapter 1.2.4, this would encourage a search for gamma rays or even neutrinos from this source. In order to link the knowledge gained from the different wavelengths, the spectral energy distribution of PKS 1814-63 is discussed in the following chapter.

3.4 Spectral energy distribution

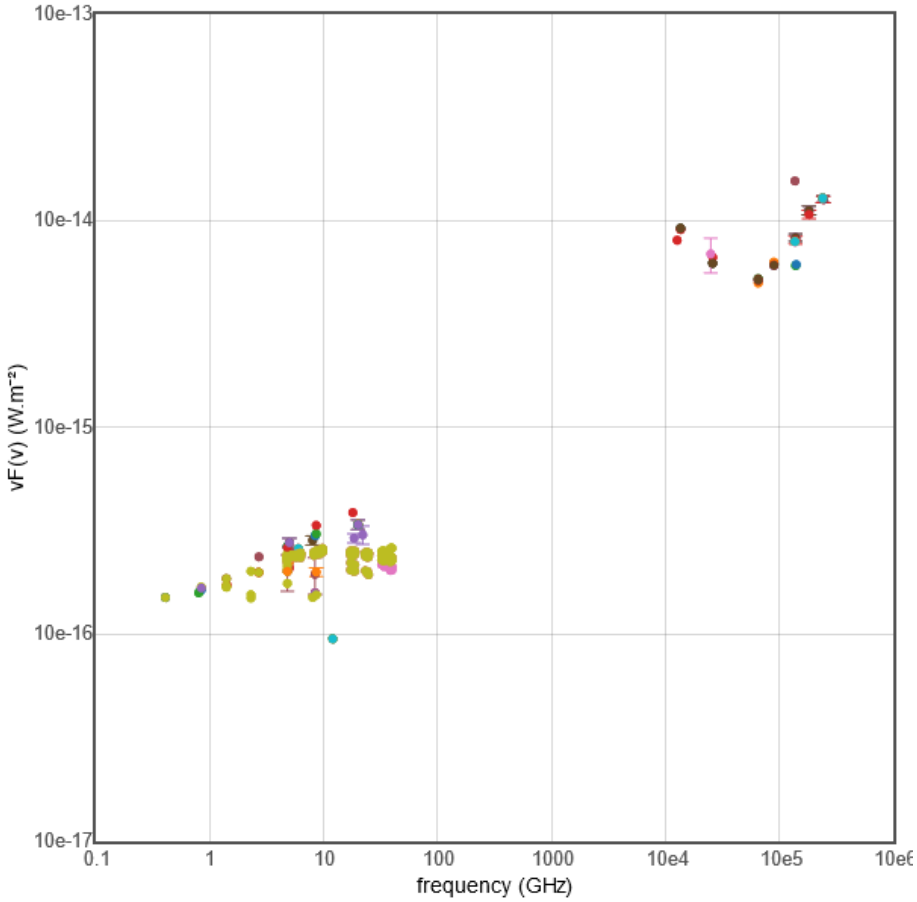

Figure 13: Spectral Energy Distribution created using the photometry viewer VizieR with focus on the galactic nucleus.

AGN are recognisable from their SED as shown in Fig. 3. A first idea of the SED of PKS 1814-63 was built for frequencies up to 10^{15} Hz with the help of the photometry viewer VizieR (see Fig. 13). When selecting the data used for this purpose, care was taken to focus as deep as possible into the nucleus of the galaxy and thus exclude measurement

points from the surroundings. In addition, care was taken to ensure that the resolution of the data-generating satellites is in the range of arcseconds to increase the confidence that the displayed emission is coming from our AGN and not from other emitters in the vicinity. The increased emission in the radio band in Fig. 13 can probably be attributed to morphological components of PKS 1814-63. As shown in chapter 3.3, a dust belt runs through the direct line of sight to the AGN. The interaction of the radiation with the dust is one way to explain the strong radio emission in the SED [36]. Since this SED has a good accuracy but does not display higher energies, the SSDC Sky Explorer tool was used to create the SED for comparison (see Fig. 14) . Here it is important to check the resolution of the individual satellites and the coordinates from which their measurements were taken, since it is not possible to focus on the galactic centre in advance.

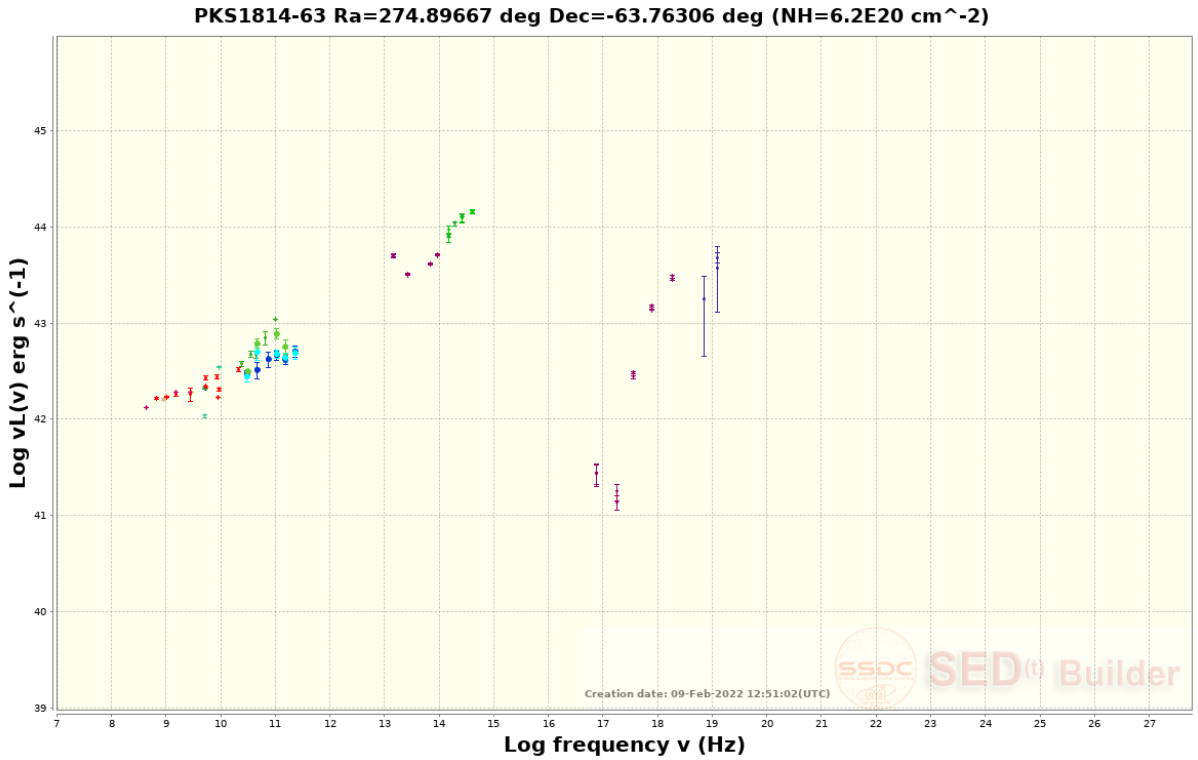

Figure 14: Spectral energy distribution created using SSDC excluding data not explicitly associated with the source.

The SSDC spectrum shows the curve already shown in Fig. 13 for low energies, with slight deviations due to the mentioned accuracy of the tool on the one hand and the larger available database of satellites on the other. Between 10^{14} Hz and 10^{15} Hz there is another peak which can be distinguished from the peak at 10^{13} Hz by a drop. This is followed by a data gap, after which a further increase can be seen in the X-ray spectrum from 10^{17} Hz, which stops at its maximum at 10^{19} Hz. Following the idea of a Seyfert-like galaxy, this spectrum compares well with the one produced by L. Giuliani et al. (2021) [36] in their work with AGN. By combining 20 classified Seyfert 2 AGN into a schematic

SED, the spectrum in Fig.15 was produced. If we now compare Fig. 13, Fig. 14 and Fig. 15 with each other, we could assign the increased radio emission to the outflow interaction discussed in chapter 3.2, since the emission is ~2 magnitudes higher than in the Seyfert 2 SED, the first peak to the dust belt, the second peak to the de-absorbed disk (accretion disk) and the increase in the X-ray could be explained by the absorbed corona emission.

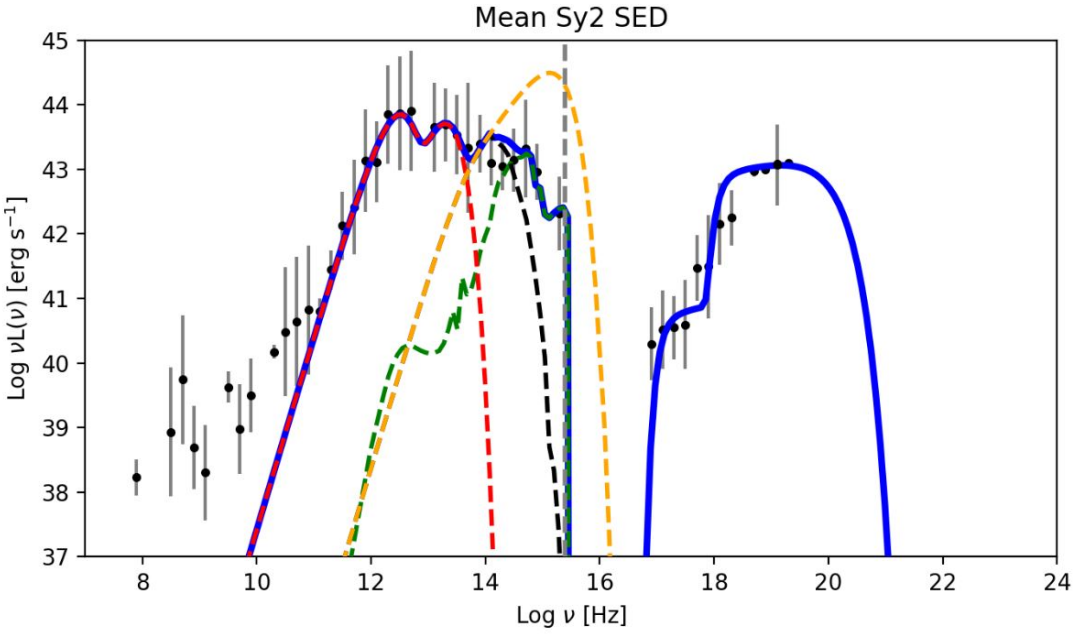

Figure 15: Mean spectral energy distribution of Seyfert 2 AGN adapted from L. Giuliani et al. (2021) [36]. The following components are to be distinguished here: The dust belt (red, dashed), the de-absorbed disk (yellow, dashed), the host galaxy (green, dashed), the absorbed disk (black, dashed). The blue solid line describes the model fit for absorption in KeV energies and in the optical band, in higher energies up to 10^{22} Hz it describes the absorbed corona emission.

Furthermore the spectrum of a Seyfert is not expected to present emission above 10^{22} Hz, but EGRET was tentatively able to measure a emission of gamma radiation at an angular separation of of 36, 39 arcmin to PKS 1814-63 during one observation, whereupon this source was associated with the EGRET source 3EG J1813-6419 in the EGRET catalogues [37]. This can be looked up in [38], published in 2001 by J. R. Mattox, R. C. Hartman and O. Reimer. Since this was a measurement of only one observation and the association is considered a weak association by P. G. Edwards et al. (2018) [22], we perform a new gamma-ray analysis in chapter 4 using data from the *Fermi*-LAT telescope. Because also the *Fermi*-LAT telescope was able to detect gamma-ray emission with a distance of 28 arcmin from PKS 1814-63. This source with the name 4FGL J1816.0-6407 appeared in earlier versions of the catalog and is there associated with the same EGRET source as well. This is probably due to the high positional error of the EGRET source of nearly one degree but a association of the *Fermi* source with PKS 1814-63 seems unlikely, since

the error on position of 4FGL 1815.6-6407 is only 0.06 deg with a certainty of 95% and PKS 1814-63 is not within this error radius. The proximity to a gamma-ray emitter and other special cases of Seyfert galaxies, where gamma and/or radio radiation could also be detected [39][40], as well as the possible generation of gamma radiation in the ISM, is the motivation for the following chapter. In the case of gamma-ray detection in the analysis, an analysis of current X-ray data would also be necessary, since the data used in SSDC originate from a time before the launch of the *Fermi* satellite. A comparison of old X-ray data with current gamma-ray data must be viewed with caution due to the variability of AGN.

4 Gamma-ray observations and data analysis

The analysis of gamma radiation in AGN allows many conclusions about the physical properties of an AGN. In the case of PKS 1814-63, there are several reasons to search for gamma radiation, as already written in the previous chapters.

4.1 Inspecting *Fermi*-LAT data

The evaluation of data from the *Fermi*-LAT is done with a Python package called Fermipy [41]. Here, the mathematical and statistical evaluation takes place automatically using commands adapted for this purpose. It is still important to know how exactly these commands handle the data sets in order to obtain comprehensible results. In the following, we will first look at the mathematical functioning of this package.
First, define the differential count rate in the instrument phase space from the convolution of the differential flux per area in the detector coming from the source [42].

$$\frac{dN}{dt\,dE\,d\hat{p}} = \int dE'\,d\hat{p}'\,R\,\frac{dN}{dt\,dE'\,d\hat{p}'\,dS} \tag{4.1}$$

Here dN depends on E, $\hat{p}$, t and R depends on E, $\frac{\hat{p}}{E'}$, $\hat{p}'$; t. Through the Instrument Response Functions (IRFs), efficiency, angular resolution, temporal scaling factors and energy resolution are also included in the differential count rate:

$$R(E,\,\frac{\hat{p}}{E'},\,\hat{p}';\,t) = T(t)A(E',\hat{p}')P(\frac{\hat{p}}{E'},\hat{p}')D(\frac{E}{E'},\hat{p}') \tag{4.2}$$

The included functions are defined as follows:
$T(t)$: Scaling factor for temporal variations, including switching off, instrument failures and more.
$A(E',\hat{p}')$: Effective detection area for photons of energy E' and arrival direction $\hat{p}'$.
$P(\frac{\hat{p}}{E'},\hat{p}')$: Probability density that a photon with energy E' and a direction $\hat{p}'$ can be

assigned to a reconstructed direction $\hat{p}$.
$D(\frac{E}{E'}, \hat{p}')$: Probability density that a photon with energy E' and a direction $\hat{p}'$ can be assigned to a reconstructed energy E.
During the mission time of the LAT, it will collect countless amounts of photons, but for most analysis we will be interested in typically a subset of only a few thousand. In that case, a full Poisson likelihood optimization is needed to estimate the model parameters for the GeV sky. The data will be too sparse in many cases to allow the use of χ^2 as test statistic. Since these counts are not correlated and one cannot therefore assign individual events to a source, Poisson statistic offers methods for assigning events to sources with their physical properties.
Now assume a model that describes the data sufficiently down to an infinite number of parameters. Again use the differential flux per unit area and call it M this time, since some parameters are unknown. These are summarised in the sum $\{a_k\}_{k=1,\ldots,m}$. The IRFs then adjust as follows:

$$J(E, \hat{p}; \{a_k\}) = \int dt\, dE'\, d\hat{p}'\, R\, M(E', \hat{p}', t; \{a_k\}) \tag{4.3}$$

From this we can calculate the expected counts in a given energy range, angle and time interval with the integral over the differential detector count rate:

$$\Lambda(\{a_k\}) = \int_{t_1}^{t_2} \int_{\Omega} \int_{E_1}^{E_2} dE\, d\hat{p}\, dt\, J(E, \hat{p}; \{a_k\}) \tag{4.4}$$

For the transition to the Poisson statistic, one defines the probability density of observing n counts with the help of the low count rates:

$$f(n, \Lambda) = \frac{\Lambda^n}{n!} e^{-\Lambda} \tag{4.5}$$

For a representative result of the probability analysis, the measured counts are compared with the expected counts. The probability is defined as the product for each pixel l of the probability densities of the observation of N_l counts taking into account the expected value $\Lambda_l(\{a_k\})$:

$$L(\{a_k\}) = \prod_l f(N_l, \Lambda_l(\{a_k\})) \tag{4.6}$$

To find the best fit set of parameters, the probability must be maximised. To do this, it is most convenient to form the logarithm, as it separates the product into sums:

$$\log\, L(\{a_k\}) = \sum_l N_l\, \log\, \Lambda_l(\{a_k\}) - \sum_l \Lambda_l(\{a_k\}) - \sum_l \log(N_l!) \tag{4.7}$$

For the best fit, the last term can now be neglected, since it does not depend on the system. Λ_l now becomes Λ_{tot} because it describes the total number of counts predicted in the model.

$$\log\ L(\{a_k\}) = \sum_l N_l\ \log\ \Lambda_l(\{a_k\}) - \Lambda_{tot}(\{a_k\}) \tag{4.8}$$

The maximum error can be used to describe a statistical error for the best fit parameters. It comes from the upper limit of a covariance matrix, described in [43] by H. Cramer (1946), [44] by R. C. Rao et al. (1945).

$$\sigma^2_{ab} = \left[-\frac{\partial^2 \log\ L}{\partial a_a \partial a_b}\bigg|_{\{\bar{a}_k\}} \right]^{-1} \tag{4.9}$$

In order to compare the theoretical model with the measured values, the residual is calculated. It is important that, in contrast to the Test Statistic (TS), it also takes negative deviations into account, which is why it is possible to make a statement about the quality of our model. The significance of the data/model at map position i,j is given by:

$$\sigma^2_{ij} = 2sgn(\bar{n}_{ij} - \bar{m}_{ij})(\ln L_p(\bar{n}_{ij}, \bar{n}_{ij}) - \ln L_p(\bar{n}_{ij}, \bar{m}_{ij})) \tag{4.10}$$

with

$$\bar{m}_{ij} = \sum_k (m_k \cdot f_k)_{ij}\ \ \wedge\ \ \bar{n}_{ij} = \sum_k (n_k \cdot f_k)_{ij}\ \ \wedge\ \ \ln\ L_p(n,m) = n\ \ln(m) - m \tag{4.11}$$

The indices represent the map position, n_k and m_k are the data and model maps at energy plane k. f_k is the normalised convolution kernel and is proportional to the expected counts cube in a given pixel. f_k is normalized such that:

$$f_{ijk} = s_{ijk} \left(\sum_{ijk} s^2_{ijk} \right)^{-1} \tag{4.12}$$

where s is the expected counts cube of a pure signal normalized to one [45]. For graphical evaluation, the residual values of the model are plotted against their coordinates. This allows a statement to be made about how well the model fits the data. The aim is to achieve a residual map that shows neither an excess nor a deficiency of photons within the region of interest.

The TS map generates an additional source component, centred on the bins in the region of interest (ROI). In contrast to the residual, only positive deviations are considered, which is why mutually negating parameters can be taken into account. With the maximum

likelihood test statistic, one proceeds as follows for each spatial bin:

$$TS = 2 \sum_k \ln L(\mu, \theta | n_k) - \ln L(0, \theta | n_k) \tag{4.13}$$

where μ is a test source normalization parameter and θ includes all parameters for the background model. These test statistics can be interpreted like a hypothesis test. One establishes the likelihood that the data of the region of interest describe the expected model well. To do this, we compare 2 scenarios. On the one hand, the Poisson distribution is used to determine the likelihood that a model in which a test source is included describes the measurement data well, and on the other hand, it is determined whether a model in which this source is not included describes it well, our null hypothesis. The logarithmic likelihood for the null hypothesis is then subtracted from the alternative model and the test statistic is formed. The higher the Test Statistic value, the higher is the probability of a detection. The empirical approximate limit value for that is a TS of 25. A statement about the significance of such a test statistic can be made with the help of Wilks' theorem. Taking into account the degrees of freedom of an analysis, this can make a comparison with the χ^2-distribution. For the TS map the evaluation of likelihood is limited to pixels in the vicinity of the test source and the background model is fixed when fitting the test source amplitude.
There are 2 different procedures to start an analysis. The binned likelihood analysis is preferred for most LAT analyses and provides good results for long time intervals with bright sources. The unbinned likelihood analysis provides a more accurate result in some cases, but requires significantly more computing power, which is why it is often only used for short time intervals. Instructions for both and the names of the commands that correspond to the mathematics can be found in [42].

4.2 Analysis and results

The data from the *Fermi*-LAT telescope were first downloaded from the server [46] with the following specified parameters. PKS 1814-63 is located at the coordinates
RA = 274.8967 ° and DEC = −63.7631 ° and the search radius was set to 20 °. In order to be able to examine as much of the available data as possible, the spans of 2008-08-04 15:43:36 – 2021-10-05 05:21:40 and 100 MeV to 300000 MeV were set for time and energy. The evaluation of the data was carried out in various ways in python 2.7, which are explained below in the order in which they were applied in the analysis. The necessary configuration files can be found in the appendix. First, the data were filtered using gtselect, it was ensured that only events with a high probability of being photons were taken into account. In this case, the following filters were used: evclass = 128 evtype = 3. A time filter was then applied using the gtmktime command to ensure

that only data in which the satellite was operating in standard data taking mode and had good data quality was used. The filter used, recommended by the LAT team, is: $(DATA\_QUAL > 0)\&\&(LAT\_CONFIG == 1)$. To take into account the dependence of the photon direction on the instrument response function, a live-time cube is calculated. The command used for this is gtlcube and is applied automatically if not already executed before using a script. Then, an analysis was run for the entire time interval and taking into account the entire energy span with the help of a script made for this purpose, which creates TS maps, residuals, bestfits and light curves by applying the fermitools. The script that summarises the commands of Fermipy for this purpose can also be found in the appendix.

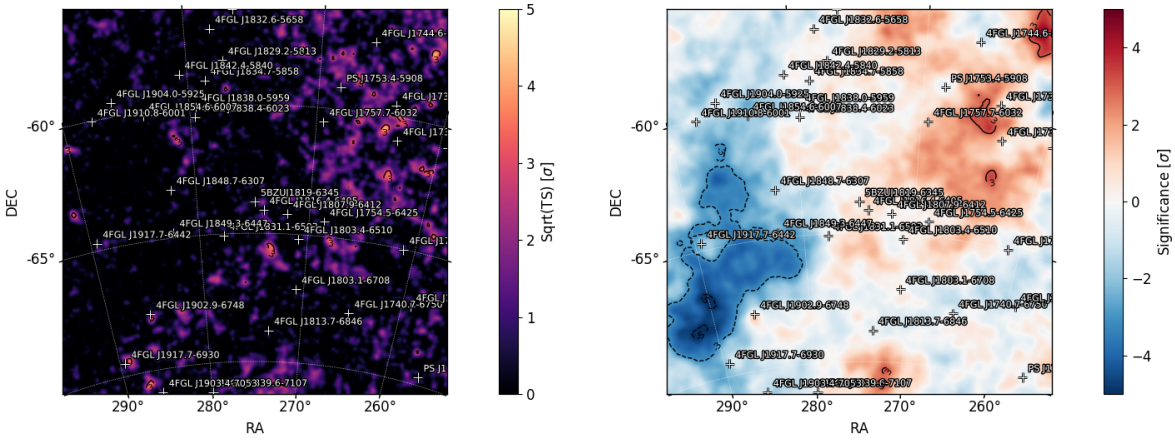

Figure 16: The left panel shows the TSmap of the region of interest around PKS 1814-63 (Here and in the following analysis shown by its name in the Blazar-Catalog 5BZUJ1819-6345). It compares the model where the source is included to a model where it is excluded to measure the likelihood of the position and photon excess.
The right panel is the residual map of the region of interest. It measures the difference of photon counts to the predicted model and plots them depending on their coordinates and if the model describes our data well, there is a significance close to zero. The spots with a significance of up to -3 are due to likely modelling problems in the diffuse component but as the close region around the source is modeled with a significance near zero, this was not taken into account any further.

For the test statistic, it creates a map of the region with an additional source component at each spatial bin. If the source emits strong gamma radiation, this is indicated in the TSmap by a strong excess consistent with our source position in the center of the ROI. The higher the excess, the higher the significance of the source and the associated probability that it is a gamma-ray emitter. Focusing on the source, the result of the TS map with the source extracted can be seen in Fig. 16 in comparison with the residual. Since

there is hardly any excess in the TSmap, it could be assumed that there is no or only weak gamma-ray emission from our target. As a next step, the gta.free_source and gta.fit function of fermipy were used to first free the fixed parameters of the source to determine the best-fit parameters then. The values for the test statistic, the spectral index and the flux upper limit are listed in table 1. For our source, we assumed a powerlaw model defined in chapter 1.2. The spectral index defined in this way indicates the slope of the spectrum. The flux upper limit describes the limit up to which the source could emit gamma rays without being detected by *Fermi*. Therefore, if we find that *Fermi* did not detect this source to a significant level, we can calculate this limit in order to obtain information about possible modelling. The TS value in table 1 is 1.89 and therefore not a detection.

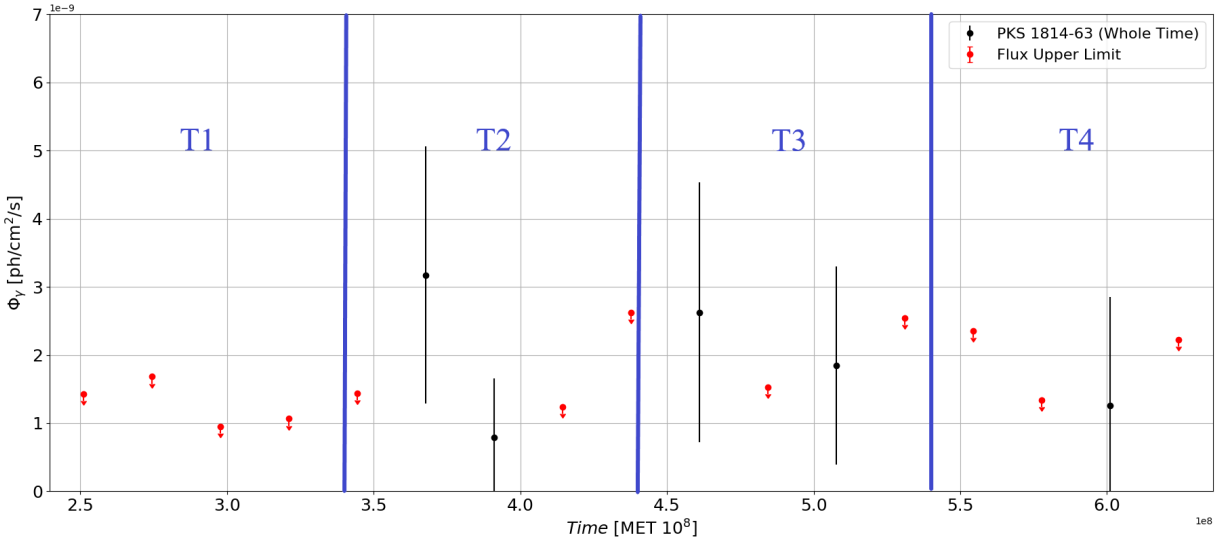

Figure 17: Light curve of PKS 1814-63 (5BZUJ1819-6345) in a time interval of 2008-08-04 15:43:36 – 2021-10-05 05:21:40. The time is given here in mission elapsed time (MET), which corresponds to the seconds since the start of the mission. Each time bin has a length of 2332800 seconds.

Since AGN are variable and the time dependence of the values must be taken into account, the light curve was then considered for the same initial values (Fig. 17). Here it can be seen that some potential gamma-ray activity might be present. In order to test whether the source may be displaying gamma-ray activity for shorter period of times due to intrinsic variability, the time span was divided into four time intervals of almost equal size, for which analyses were again carried out separately. Since only tmin and tmax were adjusted in the configuration files, they are not included in the appendix again. The time intervals with the corresponding results are listed in table 2.
For the intervals T1 and T4, the TS is zero and thus there is no detection, which is consistent with the expectation from the light curve. The spectral index is fixed at a default value of -2 for such cases. The flux upper limit indicates that gamma emission, if there is

any, will be below that limit value.
For T2, the TS value has increased slightly compared to the first analysis, but is still not sufficient to claim of a detection. The interval with the highest values in this analysis is T3. Nevertheless, the test statistic is not high enough to consider a detection. The highest TS value of 5 so far was published by M. Böck et al. (2016) [21] in the context of the TANAMI studies. Their analysis of the *Fermi*-LAT data was carried out for a narrower time interval. In addition, we investigated the time interval with the highest hint for detection, carrying out an analysis over such time span. The intervals T1 and T4 are excluded due to the lack of detection and T2 and T3 are combined (T5, shown in Fig. 18) and limited directly to the beginning and end of the flux peaks in the light curve. The results of this analysis are listed in table 3.

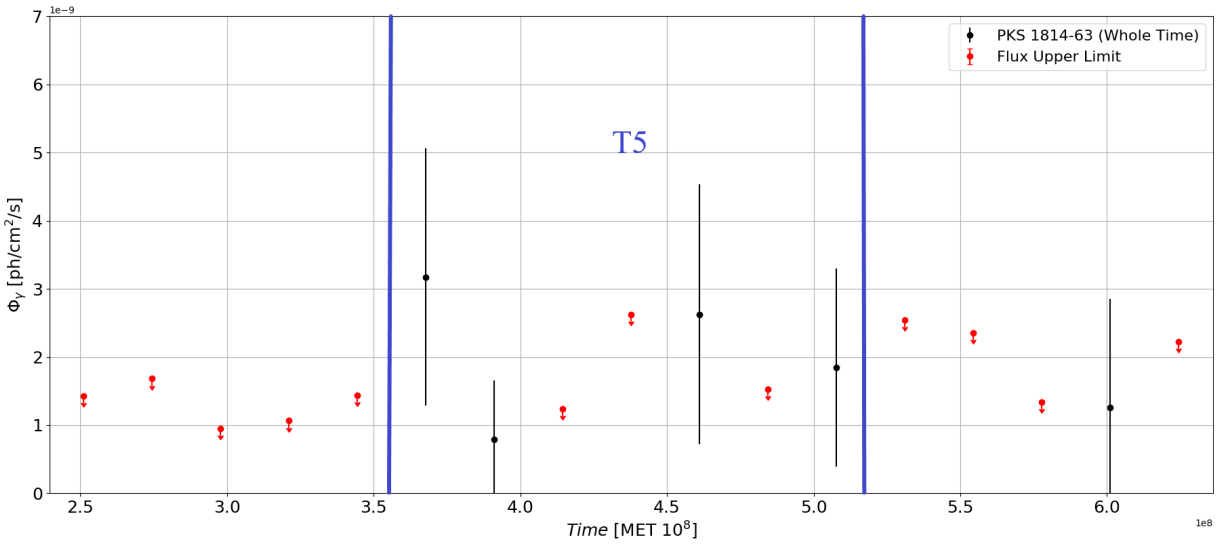

Figure 18: Same as Fig. 17.

The TS value for T5 confirms that a value of 5 could be obtained for the analysis of the TANAMI studies, but is still not large enough for possible detection. The flux upper limit no longer reaches the value determined in T3, but is higher than that in T2, which is to be expected since this time sections from both intervals were included in the calculation. As a final step in this analysis, one can include the flux upper limit for PKS 1814-63 into the SED previously created with SSDC sky explorer. This shows under which limit gamma rays could be emitted from this source but undetected for *Fermi*. This SED can be found in Fig. 19 in the appendix.

Time	Parameter	Value	Error
2008-08-04 15:43:36 -	Test Statistic	1.89	
2021-10-05 05:21:40	Spectral Index	-1.30	0.89
UTC	Flux upper limit $[10^{-11} \cdot cm^{-2} \cdot s^{-1}]$	5.31	

Table 1: Analysis result for the whole time interval.

Time	Parameter	Value	Error
2008-08-04 15:43:36 -	Test Statistic	0.00	
2011-11-03 21:43:35	Spectral Index	-2.00	0.00
UTC	Flux upper limit $[10^{-11} \cdot cm^{-2} \cdot s^{-1}]$	30.61	
2011-11-03 21:43:35 -	Test Statistic	1.97	
2015-02-02 03:43:34	Spectral Index	-1.55	0.69
UTC	Flux upper limit $[10^{-11} \cdot cm^{-2} \cdot s^{-1}]$	34.89	
2015-02-02 03:43:34 -	Test Statistic	3.95	
2018-05-03 09:43:32	Spectral Index	-1.68	0.71
UTC	Flux upper limit $[10^{-11} \cdot cm^{-2} \cdot s^{-1}]$	76.98	
2018-05-03 09:43:32 -	Test Statistic	0.00	
2021-10-05 05:21:40	Spectral Index	-2.00	0.00
UTC	Flux upper limit $[10^{-11} \cdot cm^{-2} \cdot s^{-1}]$	39.97	

Table 2: Analysis results for the time-split analysis.

Time	Parameter	Value	Error
2012-04-01 19:06:38 -	Test Statistic	6.68	
2017-06-24 12:26:35	Spectral Index	-1.53	0.52
UTC	Flux upper limit $[10^{-11} \cdot cm^{-2} \cdot s^{-1}]$	37.34	

Table 3: Analysis results for the interval with highest hint for detection.

5 Discussion

5.1 Optical spectrum

The comparison of the optical spectrum of PKS 1814-63 with the selected AGN shows many similarities with that of Seyfert galaxies and Narrow Line or Broad Line Radio Galaxies (NLRG, BLRG). Representative spectra of FSRQ and BL Lac AGN show some differences in the blue continuum with higher fluxes than PKS 1814-63 and no similarities in the case of BL Lacs as here no emission lines would be distinguishable to this extent, as is the case for PKS 1814-63, so this classification seems unlikely. For Seyfert galaxies, the Seyfert 2 galaxy and the $\gamma-$NLSy1 galaxy show the most similarities, see Fig 8. The Seyfert 2 galaxy also compares well to the optical spectrum of NLRGs and BLRGs. The classification of the Seyfert-like Galaxy is supported by the classification in the BPT diagram, see Fig. 9, for which the ratio of the intensity of characteristic emission lines was determined. Nevertheless, both quazars and radio galaxy types also occupy this area in the BPT diagram. The distinction is made by black hole mass, which is higher than for Seyfert galaxies but fits into jetted AGN samples.

5.2 Radio and morphological properties

In the radio wavelengths, PKS 1814-63 shows radio-loud properties and small jets and is classified as a CSS/CSO, due to its strongly symmetrical features and the characteristically steep rise in the radio spectrum. Through optically determined [OIII] luminosity, an intrinsically weak AGN could be assumed, which, however, does not fit the high output of radio emission. Possible explanations for this could be found, as the AGN is partially obscured by a pronounced dust belt. Interactions of the jet with this medium and/or hot particle winds from the accretion, which interact with the dust through radiation pressure and simultaneously cause the galaxy to spread out in the form of outflow material, probably significantly increase the radio emission. These properties in the radio wavelengths cannot be fully classified in either NLRG or Seyfert galaxies, which makes this source very peculiar.

5.3 Spectral energy distribution

The SEDs of PKS1814-64 show a steep region in the radio leading to a peak in the lower energy range. This is assigned to the outflow interaction by comparison with the spectrum of other Seyfert galaxies. Here, too, the similarities between Radio Galaxy and Seyfert Galaxy become apparent. The additional peak in the $10^{13}\,\mathrm{Hz} - 10^{14}\,\mathrm{Hz}$ range following a short drop was ascribed to the deabsorbed disk with the same reasoning. A gap in the lower X-ray spectrum is followed by a rise in the $10^{17}\,\mathrm{Hz} - 10^{19}\,\mathrm{Hz}$ range that can be

ascribed to absorbed corona emission, which, depending on its characteristics, drops off in the X-ray range or can be measured up to the gamma-ray range.

5.4 Gamma-ray emission

The values for the TS obtained from the analysis are consistent with previous publications that found a TS value of 0.9 to 5.0 for this source. The analysis of the *Fermi*-LAT data from 2008-2021 reported here found values from 1.89 to 6.68, taking into account different time intervals, with the last value resulting from deliberately restricting the analysis to areas with the greatest possible detection. Since the threshold value for detections is generally set at TS=25, PKS 1814-63 cannot be identified as a gamma emitter at this time with 95% confidence by *Fermi* analysis.
The light curve and the flux upper limits show a possibility for real emission from our source, which falls below the detection threshold, but also the possibility of natural fluctuations and detection of other sources in the vicinity must be taken into account. The measured values are below those of M. Böck et al (2016) [21] and R. Angioni et al (2020) [24], which can most likely be attributed to a different analysis method, as they used different point spread functions for the different energy levels, which increase the low-energy selection cut. This method has not yet been used in this work.
The spectral indices are also consistent with previous publications, which were there measured in a range of -0.8 to -1.4. Because of the quality and lack of data, these cannot be recognised as reliable indices. If gamma radiation is emitted, it is below the detection limit Fermi-LAT.

6 Conclusion

PKS 1814-63 shows many similarities with Seyfert and Narrow Line Radio galaxies. Especially the optical properties of this AGN show many similarities with these classifications, but when looking more closely at the values such as the intrinsic and bolometric luminosity, it can no longer be classified in these categories. Radio studies have also found jet properties and strong radio emission in conjunction with outflow material in the centre of the AGN. This may foster the production of gamma radiation, which is not yet detectable by Fermi, shown in the Fermi-LAT analysis. Neutrinos can also be produced in this context. The spectral energy distribution shows that the existing jet does not outshine the entire spectrum, which could be consistent with the assumption of low intrinsic power of the AGN. In addition, the individual radiating components of the AGN up to the corona emission are recognisable in the SED. Here, too, there were strong similarities with Seyfert galaxies (with the exception of the radio emission) and NLRGs. PKS 1814-63 cannot be classified with the current unification model for AGN and therefore remains a peculiar

source for the time being.

7 Outlook

In general, this source remains interesting for all wavelengths, but especially in the radio wavelengths, it would be interesting to observe possible changes in jet activity and nuclear emission in the future. Also, the X-ray emission that was publicly available in this work was limited to times before the *Fermi* telescope, so more recent observations may contribute to the overall picture. As the cumulative emission and overall properties of PKS 1814-63 are influenced by the outflow material, possible emission of gamma rays or neutrinos in the future cannot be ruled out. In future more sophisticated analysis techniques of the Fermi-LAT data may shed further light on the high-energy properties of this source.
Recently the IceCube collaboration reported an excess of neutrinos positionally consistent with the direction of NGC 1068 [47][48]. The neutrino excess is inconsistent with the background hypothesis at a ~3σ level. PKS 1814-63 shows many similarities with NGC 1068 [49], making it a good neutrino emitter candidate.

8 Acknowledgement

I would like to thank Prof. Dr. Sara Buson for the opportunity to write this thesis with her and to work with her. She persistently answered all my questions and through her extensive knowledge I was able to deepen my knowledge of AGN and the work with gamma-ray data.
I would also like to thank Raniere de Menenzes and Porf. Dr. Matthias Kadler for their support and crucial advice regarding the classification of this AGN.

Appendix

Config File:
data:
evfile : binned_events_5BZUJ.txt
scfile : ft2_5BZUJ.fits
ltcube : null

binning:
roiwidth : 15.0
binsz : 0.1
binsperdec : 8

selection:
emin : 100
emax : 300000
tmin : 239557417
tmax : 655104105
filter : $(DATA\_QUAL > 0)\&\&(LAT\_CONFIG == 1)\&\&(angsep(RA\_SUN, DEC\_SUN,$ $274.896, -63.7634) > 8.0)$
evclass : 128
evtype : 3
zmax : 90
ra : 274.896
dec : -63.7634
target : 5BZUJ1819-6345

gtlike:
irfs : P8R3_SOURCE_V2
edisp : True
edisp_disable : ['isodiff']

optimizer:
min_fit_quality: 3

lightcurve:
multithread: True
nthread: 3
free_radius: 3

shape_ts_threshold: 500000000
free_sources: ['isodiff', 'galdiff']
max_free_sources: 10
free_background: False

model:
catalogs:
- '/home/Users/LeoPfeiffer/Bachelor/Catalogs/gll_psc_v26.xml'
galdiff: '$FERMI_DIFFUSE_DIR/gll_iem_v07.fits'
isodiff: '$FERMI_DIFFUSE_DIR/iso_P8R3_SOURCE_V2_v1.txt'
sources:
- 'name': '5BZUJ1819-6345', 'ra': 274.896, 'dec': -63.7634, 'SpectrumType': PowerLaw
src_roiwidth: 20.0

Script:

```
import fermipy
import yaml
import argparse
import matplotlib as mpl
mpl.use('Agg')
from fermipy.gtanalysis import GTAnalysis
import astropy.io.fits as pyfits
from astropy.table import Table
import matplotlib.pyplot as plt
import matplotlib.image as mpimg
import errno
import sys
import numpy as np

def del_nan(gta,target):
    for i in gta.roi.sources:
        if i.name == target or i.name == 'isodiff' or i.name == 'galdiff' :
            continue
        _ts=gta.roi[i.name]['ts']
        if np.isnan(_ts)==True or _ts < 0.1:
            ihelp= '<>--<>--<> Deleting : %s %s'%(str(i.name), str(_ts))
            gta.logger.info(ihelp)
            gta.delete_source(i.name)
    return gta
def main():
    usage = "usage: %(prog)s [conFig.yaml]"
    description = "Run fermipy analysis"
    parser = argparse.ArgumentParser(usage=usage, description=description)
    parser.add_argument('--config', default='conFig.yaml')
    args = parser.parse_args()
    gta = GTAnalysis(args.config)
    outdir= gta._configdir+'/'
    gta.setup()
    source_name = gta._config['selection']['target']
    gta.logger.info(source_name)
    gta.free_sources(free=False)
    for jz in range(2):
        print 'Optimization #%i'%jz
```

```
        gta.optimize(shape_ts_threshold=500000000.0)
    gta.print_model()
    model = {'SpectrumType': 'PowerLaw', 'SpatialModel': 'PointSource'}
    srcs = gta.find_sources(model=model, sqrt_ts_threshold=5., min_separation=0.5,
           multithread=True)
    if len(srcs['sources'])>0:
        gta.setup()
        for jz in range(3):
            print '-------\nOptimization #%i\n--------'%jz
            gta.optimize(shape_ts_threshold=500000000.0)
    maps0 = gta.residmap('postfit', model=model, make_plots=True)
    tsmapNo = gta.tsmap(prefix='noExclude', make_plots=True)
    tsmap = gta.tsmap(prefix='Exclude', exclude=source_name, make_plots=True)
    gta.write_roi("bestfit", make_plots=True)
    print '*****************\nFINAL FIT VALUES\n*****************'
    gta.print_model()
    sed = gta.sed(source_name, free_background=True, make_plots=True, cov_scale=None)
    time = 3
    binsize = time*90*86400.0  # here get the bin lenght in seconds
    lc = gta.lightcurve(source_name, binsz=binsize, free_background=True,
        # save_bin_data=False, free_params=['norm'], use_local_ltcube=True,
        # use_scaled_srcmap=True, shape_ts_threshold=500000000.0,
        # outdir = 'bin_%s'%(time), prefix=time)
    print '*****************\nanalysis completed\n*****************'
    return gta
if __name__ == "__main__":
    gta = main()
```

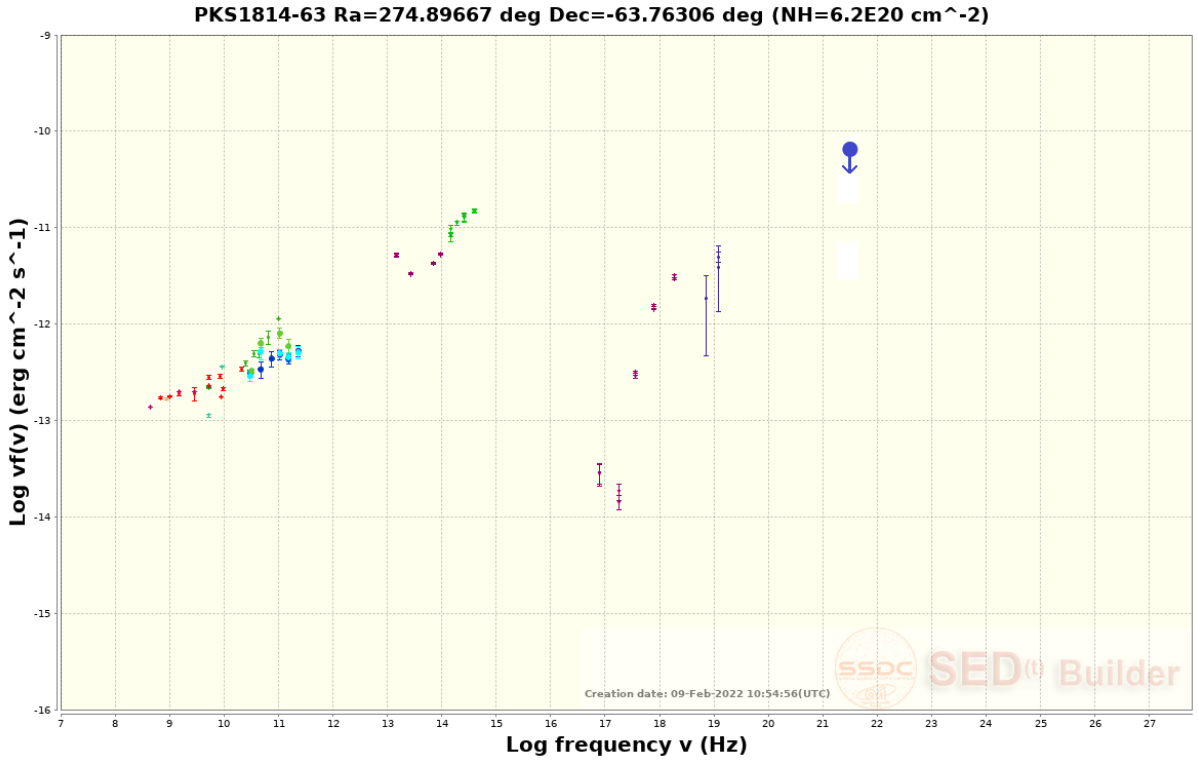

Figure 19: Spectral energy distribution created using SSDC excluding data not explicitly associated with the source. The blue arrow indicates the Flux upper limit for the *Fermi* Analysis.

References

[1] Volker Beckmann and Chris Shrader. The agn phenomenon: Open issues. Proceedings of Science, 02 2013.

[2] Paolo Padovani. On the two main classes of active galactic nuclei. Nature Astronomy, 1(8), Jul 2017.

[3] Roger Blandford, David Meier, and Anthony Readhead. Relativistic jets from active galactic nuclei. Annual Review of Astronomy and Astrophysics, 57(1):467–509, Aug 2019.

[4] P. Padovani, D. M. Alexander, R. J. Assef, B. De Marco, P. Giommi, R. C. Hickox, G. T. Richards, V. Smolčić, E. Hatziminaoglou, V. Mainieri, and et al. Active galactic nuclei: what's in a name? The Astronomy and Astrophysics Review, 25(1), Aug 2017.

[5] C Kunz. Synchrotron radiation. 1974.

[6] V. Beckman and C. Shrader. Active Galactic Nuclei. John Wiley Sons, Incorporated, 2012.

[7] G.B. Rybicki and A.P. Lightman. Radiative Processes in Astrophysics. A Wiley-Interscience publication. Wiley, 1991.

[8] Matteo Cerruti. Leptonic and hadronic radiative processes in supermassive-black-hole jets. Galaxies, 8(4):72, Oct 2020.

[9] A. A. Abdo, M. Ackermann, I. Agudo, M. Ajello, H. D. Aller, M. F. Aller, E. Angelakis, A. A. Arkharov, M. Axelsson, U. Bach, L. Baldini, J. Ballet, G. Barbiellini, D. Bastieri, B. M. Baughman, K. Bechtol, R. Bellazzini, E. Benitez, A. Berdyugin, B. Berenji, R. D. Blandford, E. D. Bloom, M. Boettcher, E. Bonamente, A. W. Borgland, J. Bregeon, A. Brez, M. Brigida, P. Bruel, T. H. Burnett, D. Burrows, S. Buson, G. A. Caliandro, L. Calzoletti, R. A. Cameron, M. Capalbi, P. A. Caraveo, D. Carosati, J. M. Casandjian, E. Cavazzuti, C. Cecchi, Ö. Çelik, E. Charles, S. Chaty, A. Chekhtman, W. P. Chen, J. Chiang, G. Chincarini, S. Ciprini, R. Claus, J. Cohen-Tanugi, S. Colafrancesco, L. R. Cominsky, J. Conrad, L. Costamante, S. Cutini, F. D'ammando, R. Deitrick, V. D'Elia, C. D. Dermer, A. de Angelis, F. de Palma, S. W. Digel, I. Donnarumma, E. do Couto e. Silva, P. S. Drell, R. Dubois, D. Dultzin, D. Dumora, A. Falcone, C. Farnier, C. Favuzzi, S. J. Fegan, W. B. Focke, E. Forné, P. Fortin, M. Frailis, L. Fuhrmann, Y. Fukazawa, S. Funk, P. Fusco, J. L. Gómez, F. Gargano, D. Gasparrini, N. Gehrels, S. Germani, B. Giebels, N. Giglietto, P. Giommi, F. Giordano, A. Giuliani, T. Glanzman, G. Godfrey, I. A. Grenier, C. Gronwall, J. E. Grove, L. Guillemot, S. Guiriec, M. A. Gurwell, D. Hadasch, Y. Hanabata, A. K. Harding, M. Hayashida, E. Hays, S. E. Healey, J. Heidt, D. Hiriart, D. Horan, E. A. Hoversten, R. E. Hughes, R. Itoh, M. S. Jackson, G. Jóhannesson, A. S. Johnson, W. N. Johnson, S. G. Jorstad, M. Kadler, T. Kamae, H. Katagiri, J. Kataoka, N. Kawai, J. Kennea, M. Kerr, G. Kimeridze, J. Knödlseder, M. L. Kocian, E. N. Kopatskaya, E. Koptelova, T. S. Konstantinova, Y. Y. Kovalev, Yu. A. Kovalev, O. M. Kurtanidze, M. Kuss, J. Lande, V. M. Larionov, L. Latronico, P. Leto, E. Lindfors, F. Longo, F. Loparco, B. Lott, M. N. Lovellette, P. Lubrano, G. M. Madejski, A. Makeev, P. Marchegiani, A. P. Marscher, F. Marshall, W. Max-Moerbeck, M. N. Mazziotta, W. McConville, J. E. McEnery, C. Meurer, P. F. Michelson, W. Mitthumsiri, T. Mizuno, A. A. Moiseev, C. Monte, M. E. Monzani, A. Morselli, I. V. Moskalenko, S. Murgia, I. Nestoras, K. Nilsson, N. A. Nizhelsky, P. L. Nolan, J. P. Norris, E. Nuss, T. Ohsugi, R. Ojha, N. Omodei, E. Orlando, J. F. Ormes, J. Osborne,

M. Ozaki, L. Pacciani, P. Padovani, C. Pagani, K. Page, D. Paneque, J. H. Panetta, D. Parent, M. Pasanen, V. Pavlidou, V. Pelassa, M. Pepe, M. Perri, M. Pesce-Rollins, S. Piranomonte, F. Piron, C. Pittori, T. A. Porter, S. Puccetti, F. Rahoui, S. Rainò, C. Raiteri, R. Rando, M. Razzano, A. Reimer, O. Reimer, T. Reposeur, J. L. Richards, S. Ritz, L. S. Rochester, A. Y. Rodriguez, R. W. Romani, J. A. Ros, M. Roth, P. Roustazadeh, F. Ryde, H. F. W. Sadrozinski, A. Sadun, D. Sanchez, A. Sander, P. M. Saz Parkinson, J. D. Scargle, A. Sellerholm, C. Sgrò, M. S. Shaw, L. A. Sigua, E. J. Siskind, D. A. Smith, P. D. Smith, G. Spandre, P. Spinelli, J. L. Starck, M. Stevenson, G. Stratta, M. S. Strickman, D. J. Suson, H. Tajima, H. Takahashi, T. Takahashi, L. O. Takalo, T. Tanaka, J. B. Thayer, J. G. Thayer, D. J. Thompson, L. Tibaldo, D. F. Torres, G. Tosti, A. Tramacere, Y. Uchiyama, T. L. Usher, V. Vasileiou, F. Verrecchia, N. Vilchez, M. Villata, V. Vitale, A. P. Waite, P. Wang, B. L. Winer, K. S. Wood, T. Ylinen, J. A. Zensus, G. V. Zhekanis, and M. Ziegler. The Spectral Energy Distribution of Fermi Bright Blazars. , 716(1):30–70, June 2010.

[10] J.R. Mattox. The sensitivity of egret to gamma-ray polarization. page 10, 1990.

[11] W. B. Atwood, A. A. Abdo, M. Ackermann, W. Althouse, B. Anderson, M. Axelsson, L. Baldini, J. Ballet, D. L. Band, G. Barbiellini, and et al. The large area telescope on thefermi gamma-ray space telescopemission. The Astrophysical Journal, 697(2):1071–1102, May 2009.

[12] G. Kanbach, D. L. Bertsch, C. E. Fichtel, R. C. Hartman, S. D. Hunter, D. A. Kniffen, B. W. Hughlock, A. Favale, R. Hofstadter, and E. B. Hughes. The project EGRET (energetic gamma-ray experiment telescope) on NASA's Gamma-Ray Observatory GRO. , 49(1-2):69–84, January 1989.

[13] R P Johnson and R Mukherjee. GeV telescopes: results and prospects for fermi. New Journal of Physics, 11(5):055008, may 2009.

[14] F. Santoro, C. Tadhunter, D. Baron, R. Morganti, and J. Holt. Agn-driven outflows and the agn feedback efficiency in young radio galaxies. Astronomy Astrophysics, 644:A54, Dec 2020.

[15] Vaidehi S. Paliya. Gamma-ray emitting narrow-line seyfert 1 galaxies: Past, present, and future. Journal of Astrophysics and Astronomy, 40(5), Oct 2019.

[16] Rafael Costero and Donald E. Osterbrock. The Optical Spectra of Narrow-Line Radio Galaxies. , 211:675–683, February 1977.

[17] J. A. Baldwin, M. M. Phillips, and R. Terlevich. Classification parameters for the emission-line spectra of extragalactic objects. , 93:5–19, February 1981.

[18] R. Morganti, J. Holt, C. Tadhunter, C. Ramos Almeida, D. Dicken, K. Inskip, T. Oosterloo, and T. Tzioumis. Pks 1814-637: a powerful radio-loud agn in a disk galaxy. Astronomy Astrophysics, 535:A97, Nov 2011.

[19] A. Tzioumis, E. King, R. Morganti, D. Dallacasa, C. Tadhunter, C. Fanti, J. Reynolds, D. Jauncey, R. Preston, P. McCulloch, S. Tingay, P. Edwards, M. Costa, D. Jones, J. Lovell, R. Clay, D. Meier, D. Murphy, R. Gough, R. Ferris, G. White, and P. Jones. A sample of southern Compact Steep Spectrum radio sources: The VLBI observations. , 392:841–850, September 2002.

[20] R. Ojha, M. Kadler, M. Böck, R. Booth, M. S. Dutka, P. G. Edwards, A. L. Fey, L. Fuhrmann, R. A. Gaume, H. Hase, S. Horiuchi, D. L. Jauncey, K. J. Johnston, U. Katz, M. Lister, J. E. J. Lovell, C. Müller, C. Plötz, J. F. H. Quick, E. Ros, G. B. Taylor, D. J. Thompson, S. J. Tingay, G. Tosti, A. K. Tzioumis, J. Wilms, and J. A. Zensus. TANAMI: tracking active galactic nuclei with austral milliarcsecond

interferometry . I. First-epoch 8.4 GHz images. , 519:A45, September 2010.

[21] M. Böck, M. Kadler, C. Müller, G. Tosti, R. Ojha, J. Wilms, D. Bastieri, T. Burnett, B. Carpenter, E. Cavazzuti, M. Dutka, J. Blanchard, P. G. Edwards, H. Hase, S. Horiuchi, D. L. Jauncey, F. Krauß, M. L. Lister, J. E. J. Lovell, B. Lott, D. W. Murphy, C. Phillips, C. Plötz, T. Pursimo, J. Quick, E. Ros, G. Taylor, D. J. Thompson, S. J. Tingay, A. Tzioumis, and J. A. Zensus. Radio and gamma-ray properties of extragalactic jets from the TANAMI sample. , 590:A40, May 2016.

[22] P. G. Edwards, R. Ojha, R. Dodson, J. E. J. Lovell, J. E. Reynolds, A. K. Tzioumis, J. Quick, G. Nicolson, and S. J. Tingay. Vlbi observations of southern gamma-ray sources. iii. Publications of the Astronomical Society of Australia, 35:e009, 2018.

[23] R. Angioni, E. Ros, M. Kadler, R. Ojha, C. Müller, P. G. Edwards, P. R. Burd, B. Carpenter, M. S. Dutka, S. Gulyaev, and et al. Gamma-ray emission in radio galaxies under the vlbi scope. Astronomy Astrophysics, 627:A148, Jul 2019.

[24] R. Angioni, E. Ros, M. Kadler, R. Ojha, C. Müller, P. G. Edwards, P. R. Burd, B. Carpenter, M. S. Dutka, S. Gulyaev, and et al. -ray emission in radio galaxies under the vlbi scope. Astronomy Astrophysics, 641:A152, Sep 2020.

[25] G. B. Taylor and A. B. Peck. Identifying compact symmetric objects in the southern sky. The Astrophysical Journal, 597(1):157–165, Nov 2003.

[26] E. Massaro, A. Maselli, C. Leto, P. Marchegiani, M. Perri, P. Giommi, and S. Piranomonte. The 5th edition of the Roma-BZCAT. A short presentation. , 357(1):75, May 2015.

[27] Ryosuke Itoh, Yousuke Utsumi, Yoshiyuki Inoue, Kouji Ohta, Akihiro Doi, Tomoki Morokuma, Koji S. Kawabata, and Yasuyuki T. Tanaka. Blazar radio and optical survey (bros): A catalog of blazar candidates showing flat radio spectrum and their optical identification in pan-starrs1 surveys, 2020.

[28] M. Karouzos, S. Britzen, A. Witzel, J. A. Zensus, and A. Eckart. Deconstructing blazars: A different scheme for jet kinematics in flat-spectrum agn. Astronomy Astrophysics, 537:A112, Jan 2012.

[29] J. F. Helmboldt, G. B. Taylor, R. C. Walker, and R. D. Blandford. A statistical description of agn jet evolution from the vlba imaging and polarimetry survey (vips). The Astrophysical Journal, 681(2):897–904, Jul 2008.

[30] F. Santoro, C. Tadhunter, D. Baron, R. Morganti, and J. Holt. Agn-driven outflows and the agn feedback efficiency in young radio galaxies. Astronomy Astrophysics, 644:A54, Dec 2020.

[31] A. Lamastra, S. Bianchi, G. Matt, G. C. Perola, X. Barcons, and F. J. Carrera. The bolometric luminosity of type 2 AGN from extinction-corrected [OIII]. No evidence of Eddington-limited sources. , 504(1):73–79, September 2009.

[32] Timothy M. Heckman, Guinevere Kauffmann, Jarle Brinchmann, Stephane Charlot, Christy Tremonti, and Simon D. M. White. Present-day growth of black holes and bulges: The sloan digital sky survey perspective. The Astrophysical Journal, 613(1):109–118, sep 2004.

[33] C. Ramos Almeida, C. N. Tadhunter, K. J. Inskip, R. Morganti, J. Holt, and D. Dicken. The optical morphologies of the 2 jy sample of radio galaxies: evidence for galaxy interactions. Monthly Notices of the Royal Astronomical Society, page no–no, Oct 2010.

[34] LAT Collaboration. Gamma rays from fast black-hole winds, 2021.

[35] P Padovani, A Turcati, and E Resconi. Agn outflows as neutrino sources: an observational test. Monthly Notices of the Royal Astronomical Society, 477(3):3469–3479,

Apr 2018.

[36] Luca Giuliani, G. Ghisellini, and Tullia Sbarrato. A new panchromatic classification of unclassified burst alert telescope active galactic nuclei. 02 2021.

[37] R. C. Hartman, D. L. Bertsch, S. D. Bloom, A. W. Chen, P. Deines-Jones, J. A. Esposito, C. E. Fichtel, D. P. Friedlander, S. D. Hunter, L. M. McDonald, P. Sreekumar, D. J. Thompson, B. B. Jones, Y. C. Lin, P. F. Michelson, P. L. Nolan, W. F. Tompkins, G. Kanbach, H. A. Mayer-Hasselwander, A. Mucke, M. Pohl, O. Reimer, D. A. Kniffen, E. J. Schneid, C. von Montigny, R. Mukherjee, and B. L. Dingus. The third EGRET catalog of high-energy gamma-ray sources. The Astrophysical Journal Supplement Series, 123(1):79–202, jul 1999.

[38] J. R. Mattox, R. C. Hartman, and O. Reimer. A quantitative evaluation of potential radio identifications for 3eg EGRET sources. The Astrophysical Journal Supplement Series, 135(2):155–175, aug 2001.

[39] W. Yuan, H. Y. Zhou, S. Komossa, X. B. Dong, T. G. Wang, H. L. Lu, and J. M. Bai. A population of radio-loud narrow-line seyfert 1 galaxies with blazar-like properties? The Astrophysical Journal, 685(2):801–827, oct 2008.

[40] A. Kreikenbohm, R. Schulz, M. Kadler, J. Wilms, A. Markowitz, C. S. Chang, B. Carpenter, D. Elsässer, N. Gehrels, K. Mannheim, C. Müller, R. Ojha, E. Ros, and J. Trüstedt. The gamma-ray emitting radio-loud narrow-line Seyfert 1 galaxy PKS 2004-447. I. The X-ray View. , 585:A91, January 2016.

[41] Matthew Wood, Regina Caputo, Eric Charles, Mattia Di Mauro, Jeffrey Magill, and Jeremy Perkins. Fermipy: An open-source python package for analysis of fermi-lat data, 2017.

[42] Fermi documentation. `https://fermi.gsfc.nasa.gov/ssc/`. Last visited 16.02.2022.

[43] Cramer, h., science 104, 450 (1946).

[44] Rao, r. c., bull. calcutta math. soc. 37, 81 (1945).

[45] Fermipy documentation. `https://fermipy.readthedocs.io/en/latest/index.html`. Last visited 13.12.2021.

[46] Fermi lat data server. `https://fermi.gsfc.nasa.gov/cgi-bin/ssc/LAT/LATDataQuery.cgi`. Last visited 16.02.2022.

[47] IceCube Collaboration, Rezvan Abbasi, J. Adams, Juan Antonio Aguilar Sánchez, M. Ahlers, M. Ahrens, Cyril Alispach, N. Amin, Karen Andeen, Travi Anderson, I. Ansseau, G. Anton, Carlos Arguelles Delgado, Spencer Axani, Xiaoqiong Bai, Aswathi Balagopal v, A. Barbano, S. Barwick, and M. Zöcklein. Icecube data for neutrino point-source searches years 2008-2018. 01 2021.

[48] M.G. Aartsen, M. Ackermann, J. Adams, J.A. Aguilar, M. Ahlers, M. Ahrens, C. Alispach, K. Andeen, T. Anderson, I. Ansseau, G. Anton, C. Argüelles, J. Auffenberg, S. Axani, P. Backes, H. Bagherpour, X. Bai, A. Balagopal, A. Barbano, S.W. Barwick, B. Bastian, V. Baum, S. Baur, R. Bay, J.J. Beatty, K.-H. Becker, J. Becker Tjus, S. BenZvi, D. Berley, E. Bernardini, D.Z. Besson, G. Binder, D. Bindig, E. Blaufuss, S. Blot, C. Bohm, M. Börner, S. Böser, O. Botner, J. Böttcher, E. Bourbeau, J. Bourbeau, F. Bradascio, J. Braun, S. Bron, J. Brostean-Kaiser, A. Burgman, J. Buscher, R.S. Busse, T. Carver, C. Chen, E. Cheung, D. Chirkin, S. Choi, K. Clark, L. Classen, A. Coleman, G.H. Collin, J.M. Conrad, P. Coppin, P. Correa, D.F. Cowen, R. Cross, P. Dave, C. De Clercq, J.J. DeLaunay, H. Dembinski, K. Deoskar, S. De Ridder, P. Desiati, K.D. de Vries, G. de Wasseige, M. de With, T. DeYoung, A. Diaz, J.C. Díaz-Vélez, H. Dujmovic, M. Dunkman, E. Dvorak,

B. Eberhardt, T. Ehrhardt, P. Eller, R. Engel, P.A. Evenson, S. Fahey, A.R. Fazely, J. Felde, K. Filimonov, C. Finley, D. Fox, A. Franckowiak, E. Friedman, A. Fritz, T.K. Gaisser, J. Gallagher, E. Ganster, S. Garrappa, L. Gerhardt, K. Ghorbani, T. Glauch, T. Glüsenkamp, A. Goldschmidt, J.G. Gonzalez, D. Grant, Z. Griffith, S. Griswold, M. Günder, M. Gündüz, C. Haack, A. Hallgren, R. Halliday, L. Halve, F. Halzen, K. Hanson, A. Haungs, D. Hebecker, D. Heereman, P. Heix, K. Helbing, R. Hellauer, F. Henningsen, S. Hickford, J. Hignight, G.C. Hill, K.D. Hoffman, R. Hoffmann, T. Hoinka, B. Hokanson-Fasig, K. Hoshina, F. Huang, M. Huber, T. Huber, K. Hultqvist, M. Hünnefeld, R. Hussain, S. In, N. Iovine, A. Ishihara, G.S. Japaridze, M. Jeong, K. Jero, B.J.P. Jones, F. Jonske, R. Joppe, D. Kang, W. Kang, A. Kappes, D. Kappesser, T. Karg, M. Karl, A. Karle, U. Katz, M. Kauer, J.L. Kelley, A. Kheirandish, J. Kim, T. Kintscher, J. Kiryluk, T. Kittler, S.R. Klein, R. Koirala, H. Kolanoski, L. Köpke, C. Kopper, S. Kopper, D.J. Koskinen, M. Kowalski, K. Krings, G. Krückl, N. Kulacz, N. Kurahashi, A. Kyriacou, M. Labare, J.L. Lanfranchi, M.J. Larson, F. Lauber, J.P. Lazar, K. Leonard, A. Leszczyńska, M. Leuermann, Q.R. Liu, E. Lohfink, C.J. Lozano Mariscal, L. Lu, F. Lucarelli, J. Lünemann, W. Luszczak, Y. Lyu, W.Y. Ma, J. Madsen, G. Maggi, K.B.M. Mahn, Y. Makino, P. Mallik, K. Mallot, S. Mancina, I.C. Mariş, R. Maruyama, K. Mase, H.S. Matis, R. Maunu, F. McNally, K. Meagher, M. Medici, A. Medina, M. Meier, S. Meighen-Berger, T. Menne, G. Merino, T. Meures, J. Micallef, D. Mockler, G. Momenté, T. Montaruli, R.W. Moore, R. Morse, M. Moulai, P. Muth, R. Nagai, U. Naumann, G. Neer, H. Niederhausen, M.U. Nisa, S.C. Nowicki, D.R. Nygren, A. Obertacke Pollmann, M. Oehler, A. Olivas, A. O'Murchadha, E. O'Sullivan, T. Palczewski, H. Pandya, D.V. Pankova, N. Park, P. Peiffer, C. Pérez de los Heros, S. Philippen, D. Pieloth, E. Pinat, A. Pizzuto, M. Plum, A. Porcelli, P.B. Price, G.T. Przybylski, C. Raab, A. Raissi, M. Rameez, L. Rauch, K. Rawlins, I.C. Rea, R. Reimann, B. Relethford, M. Renschler, G. Renzi, E. Resconi, W. Rhode, M. Richman, S. Robertson, M. Rongen, C. Rott, T. Ruhe, D. Ryckbosch, D. Rysewyk, I. Safa, S.E. Sanchez Herrera, A. Sandrock, J. Sandroos, M. Santander, S. Sarkar, S. Sarkar, K. Satalecka, M. Schaufel, H. Schieler, P. Schlunder, T. Schmidt, A. Schneider, J. Schneider, F.G. Schröder, L. Schumacher, S. Sclafani, D. Seckel, S. Seunarine, S. Shefali, M. Silva, R. Snihur, J. Soedingrekso, D. Soldin, M. Song, G.M. Spiczak, C. Spiering, J. Stachurska, M. Stamatikos, T. Stanev, R. Stein, P. Steinmüller, J. Stettner, A. Steuer, T. Stezelberger, R.G. Stokstad, A. Stößl, N.L. Strotjohann, T. Stürwald, T. Stuttard, G.W. Sullivan, I. Taboada, F. Tenholt, S. Ter-Antonyan, A. Terliuk, S. Tilav, K. Tollefson, L. Tomankova, C. Tönnis, S. Toscano, D. Tosi, A. Trettin, M. Tselengidou, C.F. Tung, A. Turcati, R. Turcotte, C.F. Turley, B. Ty, E. Unger, M.A. Unland Elorrieta, M. Usner, J. Vandenbroucke, W. Van Driessche, D. van Eijk, N. van Eijndhoven, S. Vanheule, J. van Santen, M. Vraeghe, C. Walck, A. Wallace, M. Wallraff, N. Wandkowsky, T.B. Watson, C. Weaver, A. Weindl, M.J. Weiss, J. Weldert, C. Wendt, J. Werthebach, B.J. Whelan, N. Whitehorn, K. Wiebe, C.H. Wiebusch, L. Wille, D.R. Williams, L. Wills, M. Wolf, J. Wood, T.R. Wood, K. Woschnagg, G. Wrede, D.L. Xu, X.W. Xu, Y. Xu, J.P. Yanez, G. Yodh, S. Yoshida, T. Yuan, and M. Zöcklein. Time-integrated neutrino source searches with 10 years of icecube data. Physical Review Letters, 124(5), Feb 2020.

[49] Violeta Gamez Rosas, Jacob W. Isbell, Walter Jaffe, Romain G. Petrov, James H. Leftley, Karl-Heinz Hofmann, Florentin Millour, Leonard Burtscher, Klaus Meisenheimer, Anthony Meilland, Laurens B. F. M. Waters, Bruno Lopez, Stephane

Lagarde, Gerd Weigelt, Philippe Berio, Fatme Allouche, Sylvie Robbe-Dubois, Pierre Cruzalebes, Felix Bettonvil, Thomas Henning, Jean-Charles Augereau, Pierre Antonelli, Udo Beckmann, Roy van Boekel, Philippe Bendjoya, William C. Danchi Carsten Dominik, Julien Drevon, Jack F. Gallimore, Uwe Graser, Matthias Heininger, Vincent Hocde, Michiel Hogerheijde, Josef Hron1, Caterina M. V. Impellizzeri, Lucia Klarmann, Elena Kokoulina, Lucas Labadie, Michael Lehmitz, Alexis Matter, Claudia Paladini, Eric Pantin, Jorg-Uwe Pott, Dieter Schert, Anthony Soulain, Philippe Stee, Konrad Tristram, Jozsef Varga, Julien Woillez, Sebastian Wolf, Gideon Yoffe, and Gerard Zins. Thermal imaging of dust hiding the black hole in the active galaxy ngc 1068, 2021.

Eigenständigkeitserklärung

Hiermit versichere ich, dass ich die vorliegende Arbeit selbständig verfasst, keine anderen als die angegebenen Quellen und Hilfsmittel verwendet und die Arbeit keiner anderen Prüfungsbehörde unter Erlangung eines akademischen Grades vorgelegt habe.

Würzburg, den 18. 02. 2022

Leonard Pfeiffer